Overview of aerosol optical properties over southern West Africa from DACCIWA aircraft measurements

Cyrielle Denjean[1], Thierry Bourrianne[1], Frederic Burnet[1], Marc Mallet[1], Nicolas Maury[1], Aurélie Colomb[2], Pamela Dominutti[2,*], Joel Brito[2,**], Régis Dupuy[2], Karine Sellegri[2], Alfons Schwarzenboeck[2], Cyrille Flamant[3], Peter Knippertz[4]

[1]CNRM, Université de Toulouse, Météo-France, CNRS, Toulouse, France
[2]LaMP, Université de Clermont Auvergne, Clermont-Ferrand, France
[3]LATMOS/IPSL, Sorbonne Université, UVSQ, CNRS, Paris, France
[4]Institute of Meteorology and Climate Research, Karlsruhe Institute of Technology, Karlsruhe, Germany
* Now at Wolfson Atmospheric Chemistry Laboratories, Department of Chemistry, University of York, YO10 5DD- York, UK
** Now at: IMT Lille Douai, Université de Lille, SAGE, Lille, France

Correspondence to : Cyrielle Denjean (cyrielle.denjean@meteo.fr)

Abstract. Southern West Africa (SWA) is an African pollution hotspot but a relatively poorly sampled region of the world. We present an overview of *in-situ* aerosol optical measurements collected over SWA in June and July 2016 as part as of the DACCIWA (Dynamics-Aerosol-Chemistry-Clouds Interactions in West Africa) airborne campaign. The aircraft sampled a wide range of air masses, including anthropogenic pollution plumes emitted from the coastal cities, long-range transported biomass burning plumes from Central and Southern Africa and dust plumes from the Sahara and Sahel region, as well as mixtures of these plumes. The specific objective of this work is to characterize the regional variability of the vertical distribution of aerosol particles and their spectral optical properties (single scattering albedo: *SSA*, asymmetry parameter, extinction mass efficiency, scattering Ångström exponent and absorption Ångström exponent: *AAE)*. First findings indicate that aerosol optical properties in the planetary boundary layer were dominated by a widespread and persistent biomass burning loading from the Southern Hemisphere. Despite a strong increase of aerosol number concentration in air masses downwind of urban conglomerations, spectral *SSA* were comparable to the background and showed signatures of the absorption characteristics of biomass burning aerosols. In the free troposphere, moderately to strongly absorbing aerosol layers, dominated by either dust or biomass burning particles, occurred

35 occasionally. In aerosol layers dominated by mineral dust particles, *SSA* varied from 0.81 to 0.92 at

36 550 nm depending on the variable proportion of anthropogenic pollution particles externally mixed

37 with the dust. For the layers dominated by biomass burning particles, aerosol particles were

38 significantly more light absorbing than those previously measured in other areas (e.g. Amazonia,

39 North America) with *SSA* ranging from 0.71 to 0.77 at 550 nm. The variability of *SSA* was mainly

40 controlled by variations in aerosol composition rather than in aerosol size distribution.

41 Correspondingly, values of *AAE* ranged from 0.9 to 1.1, suggesting that lens-coated black carbon

42 particles were the dominant absorber in the visible range for these biomass burning aerosols.

43 Comparison with literature shows a consistent picture of increasing absorption enhancement of

44 biomass burning aerosol from emission to remote location and underscores that the evolution of

45 *SSA* occurred a long time after emission.

46 The results presented here build a fundamental basis of knowledge about the aerosol optical

47 properties observed over SWA during the monsoon season and can be used in climate modelling

48 studies and satellite retrievals. In particular and regarding the very high absorbing properties of

49 biomass burning aerosols over SWA, our findings suggest that considering the effect of internal

50 mixing on absorption properties of black carbon particles in climate models should help better

51 assessing the direct and semi-direct radiative effects of biomass burning particles.

52

1. Introduction

54 Atmospheric aerosols play a crucial role in the climate system by altering the radiation budget

55 through scattering and absorption of solar radiation and by modifying cloud properties and

56 lifetime. Yet considerable uncertainties remain about the contribution of both natural and

57 anthropogenic aerosol to the overall radiative effect *(Boucher et al., 2013)*. Large uncertainties are

58 related to the complex and variable properties of aerosol particles that depend on the aerosol

59 source and nature as well as on spatial and temporal variations. During transport in the

60 atmosphere, aerosol particles may undergo physical and chemical aging processes altering the

61 composition and size distribution and henceforth the optical properties and radiative effects. The

62 capability of reproducing this variability in climate models represents a real challenge *(Myhre et*

63 *al., 2013; Stier et al., 2013; Mann et al., 2014)*. Therefore, intensive experimental observations in

64 both aerosol source and remote areas are of paramount importance for constraining and evaluating

65 climate models.

66

67 Key parameters from a climate perspective are the aerosol vertical distribution and respective

68 spectral optical properties. Radiative transfer codes commonly incorporated in climate models and

69 in satellite data retrieval algorithms use single scattering albedo (*SSA)*, mass extinction efficiency

70 (*MEE)* and asymmetry factor (*g*) as input parameters. These parameters depend on the aerosol size

71 distribution, the real and imaginary parts of the refractive index (*n-ik*), and the wavelength of

72 incident light, λ. The knowledge of the vertical distribution of these fundamental parameters is

73 crucial to accurately estimate the direct and semi-direct radiative effects of aerosols as well as the

74 vertical structure of atmospheric heating rates resulting from absorption by particles. Above

75 information is also required to retrieve aerosol properties (aerosol optical depth, size distribution)

76 from remote sensing data.

77

78 Southern West Africa (SWA) is one of the most climate-vulnerable region in the world , where the

79 surface temperature is expected to increase by ~3°K at the end of the century (2071-2100) in the

80 Coupled Model Intercomparison Project Phase 5 (CMIP5) *(Roehrig et al., 2013)*. It is

81 characterized by a fast-growing population, industrialization and urbanization *(Liousse et al.,*

82 *2014)*. This is particularly the case along the Guinea Coast where several already large cities are

83 experiencing rapid growth *(Knippertz et al., 2015a)*. Despite these dramatic changes, poor

84 regulation strategies of traffic, industrial and domestic emissions lead to a marked increase of

85 anthropogenic aerosol loading from multiple sources including road traffic, industrial activities,

86 waste burning, ship plumes, domestic fires, power plants, etc. Tangible evidence for regional

87 transport of anthropogenic pollutants associated with urban emissions has altered air pollution

88 from a local issue to a regional issue and beyond *(Deetz et al., 2018; Deroubaix et al. 2019)*. This

89 is particularly the case during summer when land-sea breeze systems can develop and promote the

90 transport of pollutants inland, away from the urbanized coastal strip of SWA *(Flamant et al.,*

91 *2018a)*. In addition to this anthropogenic regional pollution, SWA is impacted by a significant

92 import of aerosols from remote sources. Biomass burning mainly from vegetation fires in Central

93 Africa are advected to SWA in the marine boundary layer and aloft *(Mari et al., 2008; Menut et al.*

94 *2018; Haslett et al., 2019)*. The nearby Sahara desert and the Sahel are large sources of natural

95 wind-blown mineral dust aerosol throughout the year with a peak in springtime *(Marticorena and*

96 *Bergametti, 1996)*. Biomass burning, dust and anthropogenic pollution aerosols can be mixed

97 along their transport pathways *(Flamant et al., 2018a; Deroubaix et al. 2019)*, resulting in

98 complex interactions between physical and chemical processes and even meteorological

99 feedbacks.

100

101 In West Africa, most of the aerosol–radiation interaction studies focused on optical properties of

102 dust and biomass burning aerosols in remote regions far from major sources of anthropogenic

pollution aerosol. They include ground-based and airborne field campaigns such as DABEX (Dust and Biomass Experiment, *Haywood et al., 2008)*, AMMA (Analysis Multidisciplinary of African Monsoon, *Lebel et al., 2010)*, DODO (Dust Outflow and Deposition to the Ocean, *McConnell et al., 2008)*, SAMUM-1 and SAMUM-2 (Saharan Mineral Dust Experiment, *Heintzenberg, 2009; Ansmann et al., 2011)* and AER-D (AERosol Properties – Dust, *Ryder al. 2018)*. These projects concluded that the influence of both mineral dust and biomass burning aerosols on the radiation budget is significant over West Africa, implying that meteorological forecast and regional/global climate models should include their different radiative effects for accurate forecasts and climate simulations. Over the Sahel region, *Solmon et al. (2008)* have highlighted the high sensitivity of mineral dust optical properties to precipitation changes at a climatic scale. However, the optical properties of aerosols particles in the complex chemical environment of SWA are barely studied. This is partly due to the historically low level of industrial developments of the region. Motivated by the quickly growing cities along the Guinea Coast, the study of transport, mixing, and feedback processes of aerosol particles is therefore very important for better quantification of aerosol radiative impact at the regional scale and improvement of climate and numerical weather prediction models.

In this context, the DACCIWA (Dynamics-Aerosol-Chemistry-Clouds Interactions in West Africa, *Knippertz et al., 2015b*) campaign, designed to characterize both natural and anthropogenic emissions over SWA, provides important and unique observations of aerosols in a region much more affected by anthropogenic emissions than previously thought. A comprehensive field campaign took place in June–July 2016 including extensive ground-based *(Kalthoff et al., 2018)* and airborne measurements *(Flamant et al., 2018b)*. In this study, we present an overview of *in-situ* airborne measurements of the vertical distribution of aerosol particles and their spectral optical properties acquired with the ATR-42 French research aircraft over the Guinea Coast.

Section 2 presents the flight patterns, instrumentation and data analysis. Section 3 provides an overview of the aerosol microphysical and optical properties. The impact of aging and mixing processes on aerosol optical properties is discussed in section 4 before conclusions are presented in section 5.

2. Methodology

2.1. ATR-42 measurements overview

This analysis focuses on flight missions conducted by the ATR-42 aircraft of SAFIRE (Service des Avions Français Instrumentés pour la Recherche en Environnement - the French aircraft service for environmental research) over the Gulf of Guinea and inland. A full description of flight patterns during DACCIWA is given in *Flamant et al. (2018b)*. Here we present results from 15 flights focused on the characterization of anthropogenic pollution, dust and biomass burning plumes. The flight tracks are shown in Figure 1 and a summary of flight information is provided in Appendix 1. The sampling strategy generally consisted of two parts: first, vertical soundings were performed from 60 m up to 8 km above mean sea level (amsl) to observe and identify interesting aerosol layers. Subsequently, the identified aerosol layers were probed with the *in-situ* instruments by straight levelled runs (SLR) at fixed flight altitudes.
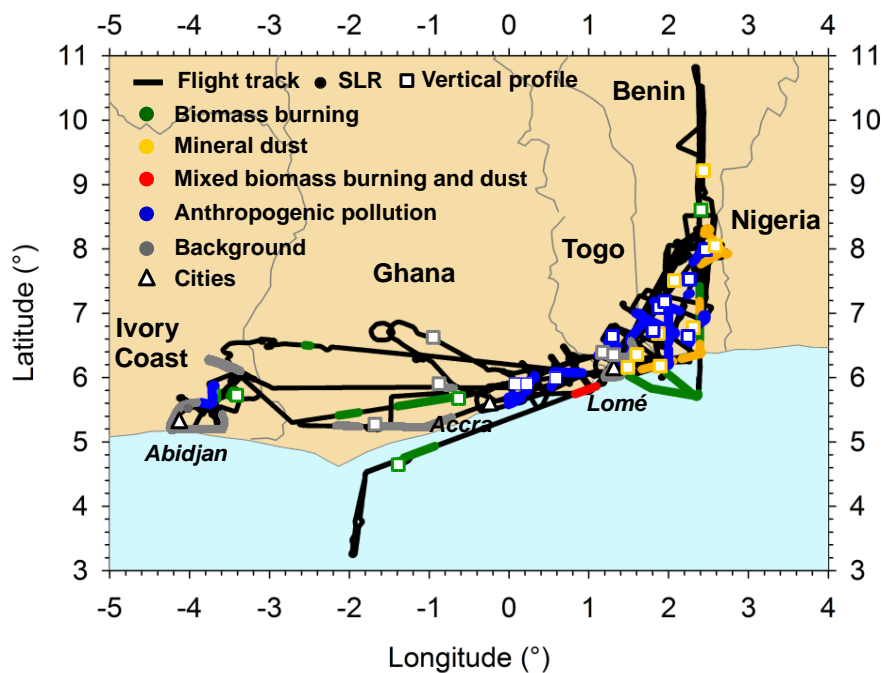
Figure 1. Tracks of the 15 flights analyzed in this study. The colors indicate aircraft flight sampling layers dominated by biomass burning (green), mineral dust (orange), mixed dust-biomass burning (red), anthropogenic pollution (blue) and background particles (grey) from both vertical profiles (squares) and straight and level runs (SLRs; dots).

The ATR-42 aircraft was equipped with a wide variety of instrumentation performing gas and aerosol measurements. The measured meteorological parameters include temperature, dew point temperature, pressure, turbulence, relative humidity, as well as wind speed and direction. Gas phase species were sampled through a rear facing ¼ inch Teflon tube. Carbon monoxide (CO) was

measured using ultra-violet and infrared analysers (PICARRO). The nitric oxide (NO) and nitrogen dioxide (NO_2) measurements were performed using an ozone chemiluminescence instrument (Thermo Environmental Instrument TEi42C with a Blue Light Converter for the NO2 conversion). On-board aerosol instruments sampled ambient air via stainless steel tubing through the Community Aerosol Inlet (CAI). This is an isokinetic and isoaxial inlet with a 50 % sampling efficiency for particles with a diameter of 5 μm *(Denjean et al., 2016).*

The total number concentration of particles larger than 10 nm (*Ntot*) was measured by a butanol-based conductive cooling type condensation particle counter (CPC, model MARIE built by University of Mainz; *Mertes, Schröder, and Wiedensohler, 1995; Russell et al., 1996; Wiedensohler et al., 1997*). The aerosol size distribution was measured using an ultra-high sensitivity aerosol spectrometer (UHSAS, DMT, 0.04 – 1 μm), a custom-built scanning mobility sizer spectrometer (SMPS, 20 - 485 nm) and an optical particle counter (OPC, GRIMM model 1.109, 0.3 – 32 μm). Instrument calibration was performed with PSL nanospheres and oil particles for diameters from 90 nm to 20 μm. The SMPS data acquisition system failed after two-third of the campaign and could not be repaired. We found the UHSAS to show false counts in the diameters below 100 nm. Therefore, these channels were disregarded in the data analysis.

The particle extinction coefficient (σ_{ext}) at the wavelength of 530 nm was measured with a cavity attenuated phase shift particle light extinction monitor (CAPS-PMex, Aerodyne Research). The particle scattering coefficients (σ_{scat}) at 450, 550 and 635 nm were measured using a TSI 3563 3-Wavelength Integrating Nephelometer and corrected for angular truncator error in the data inversion procedure using a Mie code (i.e. Section 2.3.1 and Appendix 2). The absorption coefficients (σ_{abs}) at 467, 520 and 660 nm were measured by a Radiance Research Particle Soot Absorption Photometer (PSAP). The PSAP measures changes of filter attenuation due to the collection of aerosol deposited on the filter, which were corrected for the scattering artifacts according to the *Virkkula (2010)* method. Prior to the campaign, the CAPS-PMex was evaluated against the combination of the integrating nephelometer and the PSAP. An instrument intercomparison was performed with purely scattering ammonium sulfate particles and with strongly absorbing black carbon particles (BC). Both types of aerosol were generated by nebulizing a solution of the respective substances and size-selected using a DMA. For instrument intercomparison purposes, σ_{ext} from the combination of integrating nephelometer and PSAP was adjusted to that for 530 nm by using the scattering and absorption Ångstrom exponent (*SAE* and *AAE*, respectively). The instrument evaluation showed an excellent accuracy of the CAPS-PMex

190   measurements by comparison to the integrating nephelometer and PSAP combination. The results

191   were within the ± 3 % uncertainty reported by Massoli et al. (2010) and Petzold et al. (2013) for

192   the same instrument configuration.

193

194   **2.2. Ancillary products**

195   In order to determine the history of air masses prior aircraft sampling, backward trajectories and

196   satellite images were used. The trajectories were computed using the Hybrid Single Particle

197   Lagrangian Integrated Trajectory Model (HYSPLIT) and the National Centers for Environmental

198   Prediction (NCEP) Global Data Assimilation System (GDAS) data with 0.5° horizontal resolution

199   for sequences and times of interest. We compared the backward trajectory heights with information

200   of fire burning times (e.g. MODIS Burnt Area Product) and dust release periods (e.g. Meteosat

201   Second Generation (MSG) dust RGB composite images) to assess the aerosol source regions of the

202   investigated air masses. The air masses represented by the trajectory are assumed to obtain their

203   aerosol loading from source regions when the trajectory passes over regions with significant dust

204   activation and/or fire activity at an altitude close to the surface. Trajectory calculations with

205   slightly modified initial conditions with respect to the arrival time, location and altitude were

206   performed to check the reliability of the location of source regions. Uncertainties in this approach,

207   caused by unresolved vertical mixing processes, and by general uncertainties of the trajectory

208   calculations are estimated to be in the range of 15–20 % of the trajectory distance *(Stohl et al.,*

209   *2002).*

210

211   **2.3. Data analysis**

212   In the following, extensive aerosol parameters (concentrations, scattering, absorption and

213   extinction coefficients) are converted to standard temperature and pressure (STP) using T = 273 K

214   and P = 1013.25 hPa. The STP concentration data correspond to mixing ratios, which are

215   independent of ambient pressure and temperature during the measurement. In the analysis, the data

216   were averaged over sections of SLR with homogeneous aerosol conditions outside of clouds.

217

218   **2.3.1. Derivation of aerosol microphysical and optical properties**

219   Appendix 2 and Table 1 show the iterative procedure and the equations used to calculate the

220   aerosol microphysical and optical parameters as briefly explained below.

221

222   The particle number concentration in the coarse mode (N_{coarse}) was calculated by integrating the

223   OPC size distributions over the range 1 to 5 µm. The signal to noise ratio of the OPC for particles

224   in this size range was higher than 3, which makes the instrument well suited to quantify variations
225   in N_{coarse}. The number concentration of particles in the fine mode (N_{fine}) was obtained as the
226   difference between total number concentration (N_{tot} particle diameter range above 5 nm) measured
227   by the CPC and N_{coarse}.

228

229   For optical calculations, the 3λ-σ_{abs} from the PSAP were adjusted at the 3 wavelengths measured
230   by the integrating nephelometer using the *AAE* calculated from the 3λ measured σ_{abs}. Once σ_{scat}
231   and σ_{abs} obtained at the same wavelength, an optical closure study estimated the complex refractive
232   index based on optical and size data. Optical calculations were performed using Mie theory,
233   implying a sphericity assumption, because it facilitates a quantitative comparison with past data,
234   mostly using this simplification and because most climate models assume spherical properties. The
235   retrieval algorithm consists of iteratively varying the real part of the complex refractive index *(n)*
236   from 1.33 to 1.60 and the imaginary part of the complex refractive index *(k)* from 0.000 to 0.080 in
237   steps of resolution of 0.001. *n* and *k* were fixed when the difference between calculated values of
238   σ_{scat} and σ_{abs} and measurements was below 1%. Given that the size distribution measured by the
239   UHSAS and the OPC depends on *m*, the optical-to-geometrical diameter conversion was
240   recalculated at each iteration based on the assumed *m*. The resulting number size distributions
241   from SMPS, UHSAS and OPC were parameterized by fitting four log-normal distributions and
242   used as input values in the optical calculations. Once *n* and *k* were obtained at 3λ, we estimated the
243   following optical parameters:
244   - *SAE* depends on the size of the particles. Generally, it is lower than 0 for aerosols dominated by
245   coarse particles, such as dust aerosols, but it is higher than 0 for fine particles, such as
246   anthropogenic pollution or biomass burning aerosol *(Seinfeld and Pandis, 2006; Schuster et al.,*
247   *2006).*
248   - *AAE* provides information about the chemical composition of atmospheric aerosols. BC absorbs
249   radiation across the whole solar spectrum with the same efficiency, thus it is characterized by *AAE*
250   values around 1. Conversely, mineral dust particles show strong light absorption in the blue to
251   ultraviolet spectrum leading to *AAE* values up to 3 *(Kirchstetter et al., 2004; Petzold et al., 2009).*
252   - *SSA* describes the relative importance of scattering and absorption for radiation. Thus, it indicates
253   the potential of aerosols for cooling or warming the lower troposphere.

254   - *g* describes the probability of radiation to be scattered in a given direction. Values of *g* can range
255   from −1 for entirely backscattered light to +1 for complete forward scattering light.

256   - *MEE* represents the total light extinction per unit mass concentration of aerosol. The estimates of

257   *MEE* assume mass densities of 2.65 g cm^3 for dust aerosol, 1.35 g cm^3 for biomass burning

258   aerosol, 1.7 g cm^3 for anthropogenic aerosol and 1.49 g cm^3 for background aerosol *(Hess et al.,*

259   *1998; Haywood et al., 2003a).*

Aerosol parameters	Symbol	λ (nm)	Method
Aerosol microphysical properties			
Total number concentration	N_{tot}	-	Measured by a CPC in the particle diameter range above 5 nm
Number concentration in the coarse mode	N_{coarse}	-	GRIMM size distributions integrated on the range 1 to 5 μm.
Number concentration in the fine mode	N_{fine}	-	Difference N_{tot} and N_{coarse}.
Number size distribution	dN/dlogDp	-	$dN/dlogDp = \Sigma_{i=1}^{4} (N_{tot,i} \ exp(-(logD_p - logD_{p,g,i})^2/(2 \ log \ \sigma_i))/(\sqrt{2} \ log \ \sigma_i))$ with $N_{tot,i}$ the integrated number concentration, $D_{p,g,i}$ the geometric median diameter and σ_i geometric standard deviation for each mode i
Volume size distribution	dV/dlogDp	-	$dV/dlogDp = \Sigma_{i=1}^{4} (N_{tot,i} \ D_p^3 \pi/6 \ exp(-(logD_p - logD_{p,g,i})^2/(2 \ log \ \sigma_i))/(\sqrt{2} \ log \ \sigma_i))$
Aerosol optical properties			
Scattering coefficient	σ_{scat}	450, 550, 635	Measured by the integrating nephelometer and corrected for truncator error
Absorption coefficient	σ_{abs}	467, 520, 660	Measured by the PSAP and corrected for filter based artefacts
Extinction coefficient	σ_{ext}	530	Measured by the CAPS-PMex
Scattering Ångström exponent	SAE	450 to 700	Calculated from the integrating nephelometer measurements : $SAE = -ln (\sigma_{scat}(450)/\sigma_{scat}(700)) / ln (450/700)$
Absorption Ångström exponent	AAE	440 to 660	Calculated from the PSAP measurements : $AAE = -ln(\sigma_{abs}(467)/\sigma_{abs}(660)) / ln (467/660)$
Complex refractive index	n	450, 550, 660	Inversion closure study using Mie theory (Fig. A2) $m(\lambda) = n(\lambda)-ik(\lambda)$
Single scattering albedo	SSA	450, 550, 660	Inversion closure study using Mie theory (Fig. A2) $SSA(\lambda) = \sigma_{scat}(\lambda)/\sigma_{ext}(\lambda)$
Mass extinction efficiency	MEE	450, 550, 660	Inversion closure study using Mie theory (Fig. A2) $MEE(\lambda) = \sigma_{ext}(\lambda)/C_m$ with C_m the aerosol mass concentration
Asymmetry parameter	g	450, 550, 660	Inversion closure study using Mie theory (Fig. A2) $g(\lambda) = 1/2 \int_0^\pi cos(\Theta)sin(\Theta)P(\Theta,\lambda)d(\Theta)$ with $P(\Theta,\lambda)$ the scattering phase function and Θ the scattering angle.

261   **Table 1. Aerosol microphysical and optical properties derived in this work**

262

263 **2.3.2. Classification of aerosols plumes**

264 Data were screened in order to isolate plumes dominated by anthropogenic pollution from urban

265 emissions, biomass burning and mineral dust particles, resulting in a total number of 19, 12 and 8

266 genuine plume interceptions, respectively, across the 15 flights. As shown in Figure 2,

267 identification of the plumes was based on a combination of CO and NO_x (sum of NO and NO_2)

268 concentrations, as well as *AAE* and *SAE* that have been shown to be good parameters for

269 classifying aerosol types *(Kirchstetter et al., 2004; Petzold et al., 2009)*. The classification was

270 then compared with results from the back trajectory analysis (Figure 3) and satellite images

271 described in section 2.2.
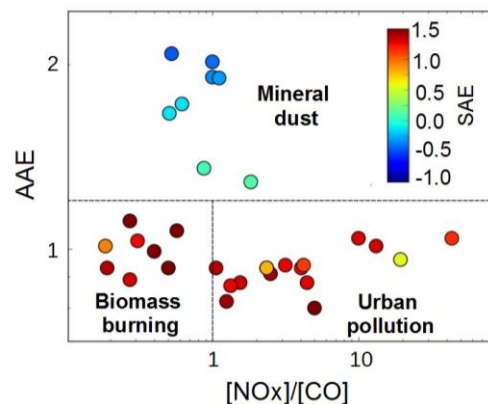
272

273 **Figure 2. Absorption Ångström Exponent (AAE) as a function of the ratio NO_x to CO. The**
274 **markers are colored according to the Scattering Ångström Exponent (SAE). Classification of**
275 **mineral dust, biomass burning and urban pollution particles has been added to the figure.**
276

277 The guidelines for classification are as follows:

278 - *Anthropogenic pollution*: *SAE* was beyond threshold 0, indicating a large number fraction of

279 small particles in urban plumes, and CO and NO_x concentrations 2 times higher than the

280 background concentrations. During the DACCIWA campaign background CO and NO_x values

281 were around 180 ppb and 0.28 ppb, respectively. The trajectories show large differences in the

282 flow patterns and source regions with urban plumes originating from the polluted cities of Lomé,

283 Accra and Abidjan. The aircraft sampling over land mostly followed the north-eastward direction

284 (Figure 3d).

285 - *Biomass burning*: The criteria are the same as for urban pollution plumes except that trajectories

286 track theses plumes back to active fire hotspots as observed by MODIS and the ratio NO_x to CO

287 was set below 1. CO and NO_x are byproducts of combustion sources but CO is preserved longer

288 along the plume when compared with NO_x, which makes the ratio NO_x to CO a good indicator for

289 distinguishing fresh anthropogenic pollution plumes from biomass burning plumes transported

290 over long distances *(Wang et al., 2002; Silva et al., 2017)*. During this time of the year, most of the

291 forest and grassland fires were located in Central and Southern Africa (Figure 3a).

292 - *Mineral dust*: *AAE* higher than 1 indicates a large mass fraction of mineral dust and a *SAE* below

293 0 indicate a high effective particle diameter. The source region of the dust loaded air masses was

294 located in the Saharan desert and in the Sahel (Figure 3b).

295 - *Dust and biomass burning mixing:* Combining remote sensing observations and model

296 simulations, *Flamant et al. (2018a)* identified a biomass burning plume mixed with mineral dust.

297 This agrees well with the measured *AAE* of 1.2 and *SAE* of 0.3 observed in this layer. *Menut et al.*

298 *(2018)* have shown that one of the transport pathways of biomass burning aerosols from Central

299 Africa was associated with northward advection towards Chad and then westward displacement

300 linked to the African Easterly Jet. The plume originated from a broad active biomass burning area

301 including Gabon, the Republic of Congo and the Democratic Republic of Congo and passed over

302 areas with strong dust emissions further north within 1–3 days before being sampled by the aircraft

303 (Figure 3c).

304 - *Background:* We refer to background conditions as an atmospheric state in the boundary layer

305 without the detectable influence of mineral dust, biomass burning or local anthropogenic sources.

306 Most back trajectories originated from the marine atmosphere and coastal areas south of the

307 sampling area.
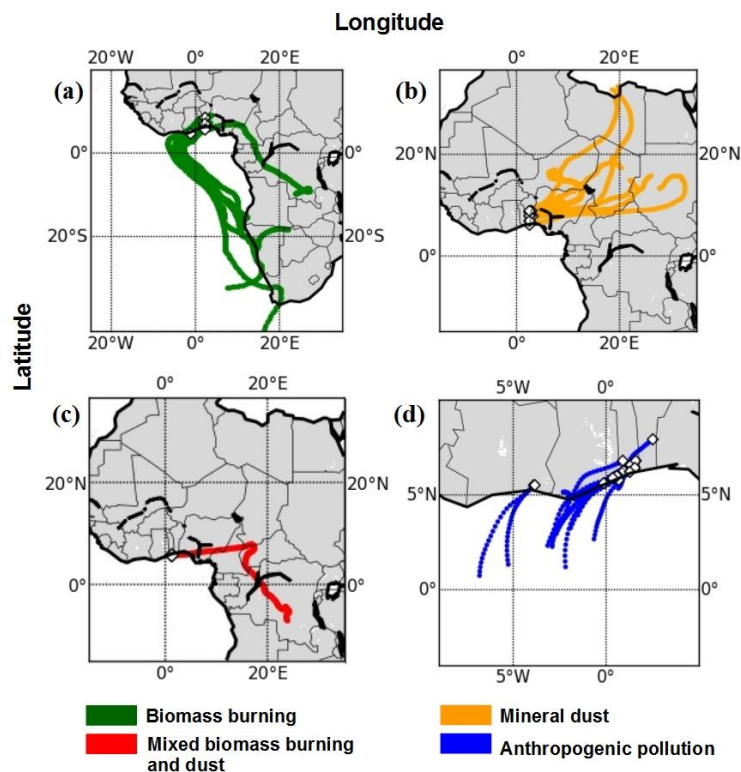
3.1. Aerosol vertical distribution

Figure 4 shows a statistical analysis of N_{fine}, N_{coarse} and σ_{ext} derived from the *in-situ* measurements of vertical profiles. The aerosol vertical structure is strongly related to the meteorological structure of the atmosphere (see *Knippertz et al., 2017* for an overview of the DACCIWA field campaign*)*. Therefore wind vector and potential temperature profiles acquired with the aircraft have been added to Figure 4 as a function of the dominating aerosol composition, introduced in Figure 1. The data from individual vertical profiles were merged into 200 m vertical bins from the surface to 6 km amsl. The profiles were calculated using only individual profiles obtained outside of clouds.
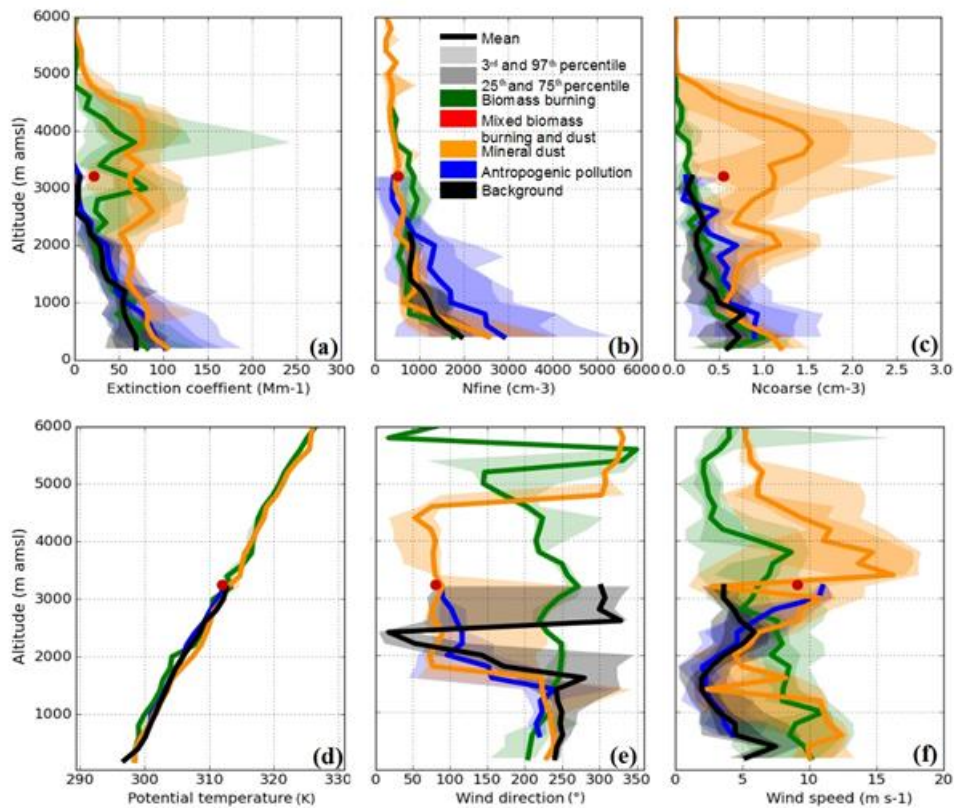
Figure 4. Vertical layering of aerosols and meteorological variables for profiles for which aerosols dominated by biomass burning (green), dust (orange), mixed dust-biomass burning (red), anthropogenic pollution (blue) and background particles (black) were detected. The panels show profiles of (a) the extinction coefficient at 530 nm, (b) the particle number concentration in the range $0.005 < D_p < 1$ μm, (c) the particle number concentration in the range $1 < D_p < 5$ μm, (d) potential temperature, (e) the wind direction and (f) the wind speed. The colored areas represent the 3th, 25th, 75th and 97th percentiles of the data. The mixed dust-biomass burning plume is represented by a dot because it is derived from measurements during a SLR.

330   The observed wind profiles highlight the presence of several distinct layers in the lower
331   troposphere. For cases related to dust, urban pollution and background condition, we clearly
332   observe the monsoon layer up to 1.5 km amsl which is characterized by weak to moderate wind
333   speeds (2 to 10 m s^{-1}, the later corresponding to dust cases) and a flow from the southwest (220-
334   250°). In all three air mass regimes, the monsoon layer is topped by a 500 to 700 m deep layer
335   characterised by a sharp wind direction change (from south-westerly to easterly). Weak wind
336   speeds (less than 5 m s^{-1}) are observed in urban pollution and background conditions, while higher
337   wind speeds are observed in the dust cases. Above 2.5 km amsl, the wind speed increases in the
338   urban pollution and dust cases and the wind remains easterly, indicating the presence of the
339   African easterly jet with its core typically farther north over the Sahel (Figure 8 in *Knippertz et al.,*
340   *2017* for the latitudinal variations of the African easterly jet during the DACCIWA field phase).
341   The maximum easterlies are observed in the dust cases slightly below 3.5 km amsl (> 15 m s^{-1}).
342   For the background cases, the wind above the shear layer shifts to north-westerly and remains
343   weak (~i.e. 5 m s^{-1}). Overall, the wind profile associated with the biomass burning cases is quite
344   different from the other three cases, with a flow essentially from the south-southwest below 5 km
345   amsl and higher wind speeds in the lower 2 km amsl than above, and a secondary maximum of 7
346   m s^{-1} at 4 km amsl.

347

348   The vertical distribution of aerosol particles was very inhomogeneous, both across separate
349   research flights and between individual plumes encountered during different periods of the same
350   flight. Measurements of aerosols within this analysis cover a broad geographic region, as shown in
351   Figure 1, which may explain some of the variability. SWA is subject to numerous anthropogenic
352   emission sources (e.g. road traffic, heavy industries, open agriculture fires, etc.) coupled to
353   biogenic emissions from the ocean and forests. These resulting large emissions are reflected in the
354   high variability of σ_{ext}, N_{fine} and N_{coarse} in the lower troposphere over SWA. Below 2.5 km amsl, σ_{ext}
355   showed a large heterogeneity with values ranging from 35 to 188 Mm^{-1} between the 3rd and 97th
356   percentile and a median value of 55 Mm^{-1}. The variability of σ_{ext} values was slightly enhanced near
357   the surface and was correlated to N_{fine} and N_{coarse} which ranged from 443 to 5250 cm^{-3} and from
358   0.15 to 1.6 cm^{-3}, respectively. Maximum surface σ_{ext} was recorded in the anthropogenic pollution
359   plume of Accra where high N_{fine} was sampled. The aerosol vertical profile is strongly modified
360   during biomass burning and dust events. The dust plume extends from 2 to 5 km amsl, and is
361   associated with transport from the dust sources in Chad and Sudan (see Figure 3) with the midlevel
362   easterly flow. The biomass burning plume extends from 1.5 to 5 km amsl and is associated with
363   transport from the southwest in a layer of enhanced wind speed just below 4 km amsl as discussed

364 above. Both layers showed enhanced σ_{ext} with median values of 68 Mm^{-1} (p_{03} = 12 Mm^{-1}; p_{97} = 243

365 Mm^{-1}) in biomass burning plumes and 78 Mm^{-1} (p_{03} = 45 Mm^{-1}; p_{97} = 109 Mm^{-1}) in dust plumes.

366 As expected, the extinction profile was strongly correlated to N_{fine} for biomass burning layers and

367 N_{coarse} for dust layers.

368

369 A prominent feature in the vertical profiles is the presence of fine particles up to 2.5 km amsl

370 outside of biomass burning or dust events. $\sigma_{ext,}$ N_{fine} and N_{coarse} continuously decrease with altitude,

371 most likely due to vertical mixing of local emissions from the surface to higher levels. Therefore,

372 the regional transport of locally emitted aerosols was not limited to the surface but occurred also at

373 higher altitude. Recently, numerical tracer experiments performed for the DACCIWA airborne

374 campaign period have demonstrated that a combination of land–sea surface temperature gradients,

375 orography-forced circulation and the diurnal cycle of the wind along the coastline favor the

376 vertical dispersion of pollutants above the boundary layer during daytime *(Deroubaix et al., 2019;*

377 *Flamant et al., 2018a)*. Because of these complex atmospheric dynamics, aerosol layers transiting

378 over the Gulf of Guinea in the free troposphere could be contaminated by background or urban

379 pollution aerosols from the major coastal cities.

380

381 **3.2. Aerosol size distribution**

382 Figure 5a shows the range of variability of the number and volume size distributions measured

383 during DACCIWA. These are extracted from the SLRs identified in Fig.1. Figure 5b shows the

384 same composite distribution normalized by CO concentration in order to account for differences in

385 the amount of emissions from combustion sources.

386
387
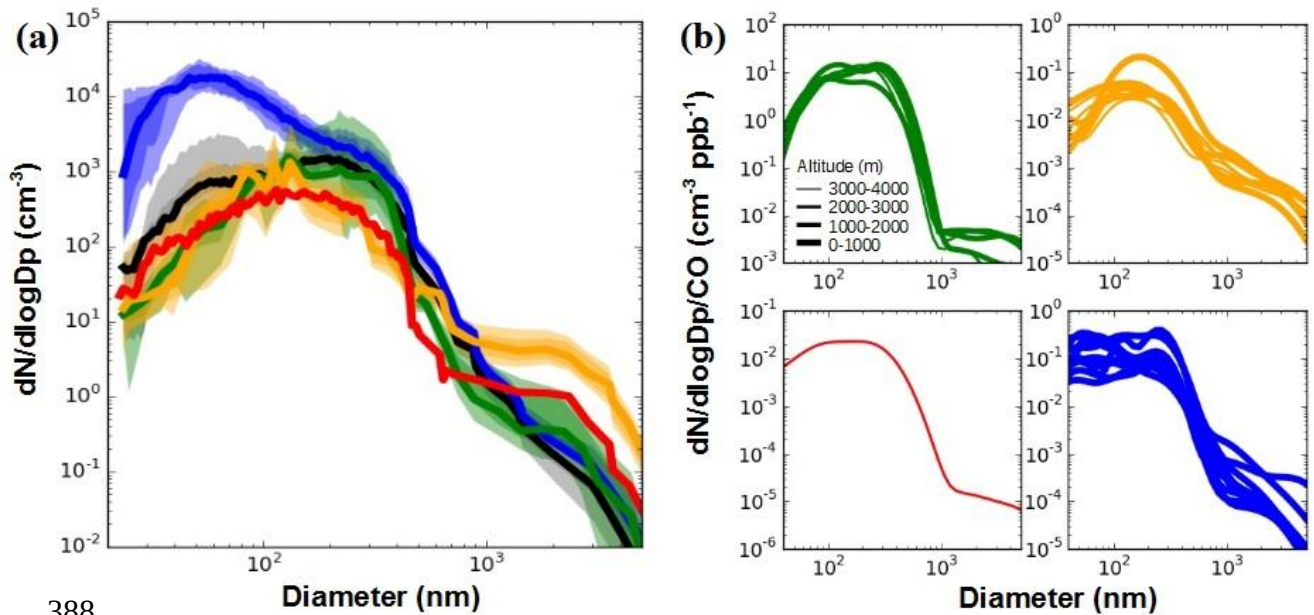
388
389 **Figure 5. (a) Statistical analysis of number size distributions with colored areas representing**
390 **the 3th, 25th, 75th and 97th percentiles of the data and (b) number size distributions normalized**
391 **to CO for plumes dominated by biomass burning (green), dust (orange), mixed dust-biomass**
392 **burning (red), anthropogenic pollution (blue) and background particles (black). In panel b,**
393 **the line thickness is scaled by the altitude of the aerosol plume.**
394

395 Considerable variability in the number concentration of the size distributions, up to approximately
396 2 orders of magnitude, was observed for a large fraction of the measured size range. The size
397 distributions varied both for different aerosol types and for a given aerosol class. This reflects the
398 relative wide range of different conditions that were observed over the region, both in terms of
399 sources, aerosol loading, and lifetimes of plumes.
400

401 In particular for ultrafine particles with diameters below 100 nm, large differences were observed,
402 with an increase as large as a factor of 50 in urban plumes, which reflects concentration increase
403 from freshly formed particles. Interestingly elevated number concentrations of these small-
404 diameter particles were also observed in some dust layers. Comparing the particle size distribution
405 of the different dust plumes sampled during the field campaign, a variation as large as a factor of
406 20 in the number concentration of ultrafine particles is found (i.e. Figure 4). Their contribution
407 decreased with height as reflected by higher small particle number recorded in dust plumes below
408 2.5 km amsl (Figure 4b and 5b). As the composite urban size distributions showed a relatively
409 similar ultrafine mode centered at 50 nm, dust layers have most likely significant contributions
410 from anthropogenic pollution aerosol freshly emitted in SWA. The ultrafine mode was not

observed in biomass burning size distributions, even though dust and biomass burning plumes were sampled in the same altitude range. We interpret this observation with dust plumes transported below 2.5 km amsl that were sampled over the region of Savè (8°01'N, 2°29'E; Benin) near the identified urban air mass transported northeastwards from Lomé and/or Accra and which may have collected significant fresh pollution on their way, whereas biomass burning plumes collected at the same altitude and sampled over Ivory Coast south of the Abidjan pollution plumes may not have been affected by significant direct pollution (Figure 1).

The accumulation mode was dominated by two modes centered at $D_{p,g}$ ~ 100 and 230 nm depending on the aerosol plume. The particle size distributions for biomass burning plumes were generally dominated by an accumulation mode centered at $D_{p,g}$ ~ 230 nm. Despite the relative wide range of sources and lifetimes of the biomass burning plumes sampled throughout the campaign (Figure 3), the $D_{p,g}$ in the accumulation mode showed little variation ($D_{p,g}$ from 210 to 270 nm) between the plumes. Similarly, previous field studies found accumulation mode mean diameters from 175 to 300 nm for aged biomass burning plumes, regardless of their age, transport time and source location *(Capes et al., 2008; Janhäll et al., 2010; Weinzierl et al., 2011; Sakamoto et al., 2015; Carrico et al. 2016)*. The coagulation rate can be very high in biomass burning plumes and can shape the size distribution over a few hours (*Sakamoto et al., 2016*). It is worth noting that in the biomass burning and dust size distributions there is a persistent particle accumulation mode centered at ~100 nm that exceeds the amount of particles centered at 230 nm in some layers. This small mode is unlikely to be related to long-range transport of biomass burning and Saharan dust emissions, as it would be expected that particles in this size range would grow to larger particles through coagulation relatively quickly. As similar concentrated accumulation modes of particles have been observed in background plumes, it suggests the entrainment of background air from the boundary layer in dust and biomass burning plumes.

The number concentration of large super-micron particles was strongly enhanced in the mineral dust layers. The peak number concentration displayed a broad shape at $D_{p,g}$ ~ 1.8 μm, which is comparable to literature values of other long-range transported dust aerosols *(Formenti et al., 2011a; Weinzierl et al., 2011; Ryder et al., 2013; Denjean et al., 2016; Liu et al., 2018)*. The super-micron mode of the dust plume is expected to be impacted by the mixing with other particles in case of an internal mixing, which should somewhat increase the particle size. The relatively homogeneous $D_{p,g}$ in the coarse mode of dust reported here ($D_{p,g}$ from 1.7 to 2.0 μm) suggests low internal mixing with other atmospheric species. Besides, the volume size distribution in urban

445 plumes showed significant presence (~ 65% of the total aerosol volume) of large particles with
446 diameters of ~ 1.5 – 2 μm, which were also observed in background conditions. We measured
447 *AAE* in the range 0.7-1 in anthropogenic pollution plumes (Figure 2), which suggests negligible
448 contribution of mineral dust in these plumes. This coarse mode has most likely significant
449 contributions from sea salt particles, as plumes arriving from the cities were transported at low
450 altitude over the ocean (Fig. 3).

451

3.3. Aerosol optical properties

453 *SSA* is one of the most relevant intensive optical properties because it describes the relative
454 strength of the aerosol scattering and absorption capacity and is a key input parameter in climate
455 models *(Solmon et al., 2008)*. Figure 6 shows the spectral *SSA* for the different SLRs considered in
456 this study.

457
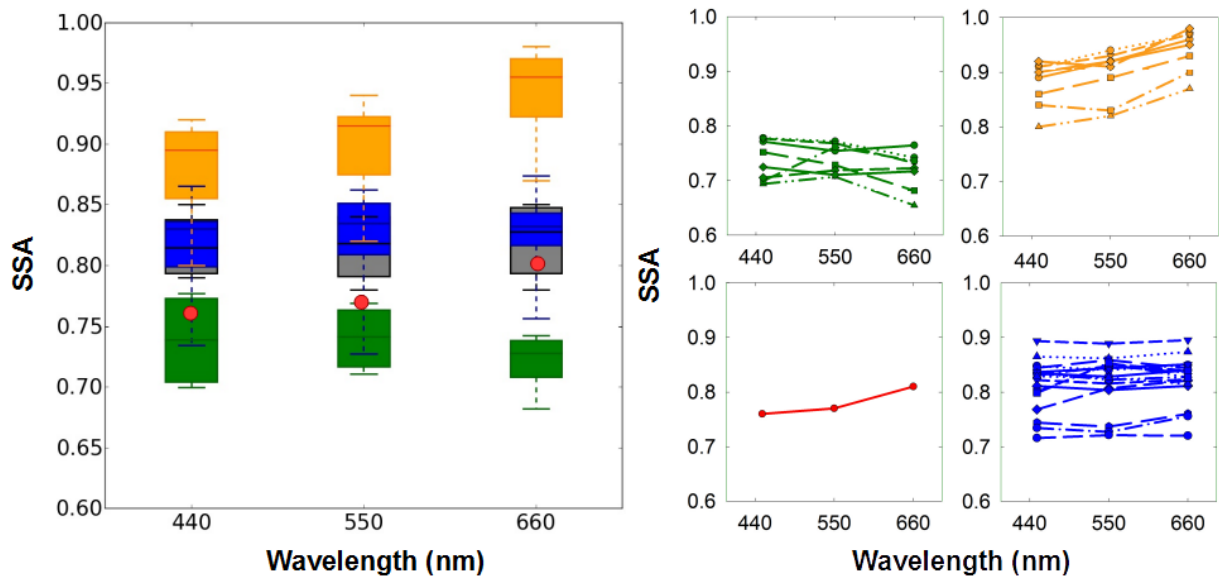
Figure 6. (a) Statistical analysis of single scattering albedo at 450, 550 and 660 nm for plumes dominated by biomass burning (green), dust (orange), mixed dust-biomass burning (red), anthropogenic pollution (blue) and background particles (black). The boxes enclose the 25th and 75th percentiles, the whiskers represent the 5th and 95th percentiles and the horizontal bar represents the median. (b) Spectral SSA for the different individual plumes considered in this study. The mixed dust-biomass burning plume is represented by a dot because it is derived from measurements during only one SLR.

465

466 The highest absorption (lowest *SSA*) at all three wavelengths was observed for biomass burning
467 aerosols. *SSA* values ranged from 0.69–0.78 at 440 nm, 0.71–0.77 at 550 nm and 0.65–0.76 at 660
468 nm. This is on the low side of the range of values (0.73–0.93 at 550 nm) reported over West Africa

469   during DABEX for biomass burning plumes mixed with variable proportion of mineral dust

470   *(Johnson et al., 2008)*. No clear tendency was found for the spectral dependence of *SSA*, which in

471   some of the cases decreased with wavelength and in others were very similar to each other at all

472   three wavelengths.

473

474   *SSA* values of anthropogenic pollution aerosols were generally intermediate in magnitude with

475   median values of 0.81 at 440 nm, 0.82 at 550 nm and 0.82 at 660 nm. Our data show that the value

476   of *SSA* varied significantly for the different plumes. Some pollution aerosols absorb almost as

477   strongly as biomass burning aerosols with *SSA(550nm)* values as low as 0.72, whereas the highest

478   *SSA(550nm)* value observed was 0.86. In addition, the absorption properties of urban aerosol

479   varied greatly between the sampled plumes for smoke of apparent same geographic origin. For

480   example, we measured *SSA(550nm)* values from 0.72 to 0.82 in the Accra pollution outflow. The

481   variability in SSA values may be due to the possible contribution of emissions from different cities

482   to the sampled pollution plumes *(Deroubaix et al., 2019)*, thus having different combustion

483   sources and chemical ages. The flat spectral dependence of SSA appears to be anomalous for

484   anthropogenic pollution aerosols, as SSA has been shown to decrease with increasing wavelength

485   for a range of different urban pollution plumes *(Dubovick et al., 2002; Petzold et al., 2011; Di*

486   *Biagio et al., 2016; Shin et al., 2019).*

487

488   The magnitude of *SSA* increased at the three wavelengths when dust events occurred. Large

489   variations in *SSA* were obtained with values ranging from 0.76–0.92 at 440 nm, 0.81–0.94 at 550

490   nm and 0.81–0.97 at 660 nm. The measurement of *SSA* is highly dependent on the extent to which

491   the coarse mode is measured behind the aerosol sampling inlet. *Denjean et al. (2016)* found that

492   the absolute error associated with *SSA, g and MEE* of dust aerosols due to the CAI inlet is in the

493   range covered by the measurement uncertainties. However, different aerosol inlet systems were

494   used during previous field campaigns, which makes comparison of our results with previous

495   measurements difficult. Overall, compared with the literature for transported dust, lower values

496   were obtained in the present study for few cases. For example, *Chen et al. (2011)* reported

497   SSA(550 nm) values of 0.97±0.02 during NAMMA (a part of AMMA operated by NASA) using

498   an inlet with a comparable sampling efficiency. The lower values from DACCIWA reflect

499   inherently more absorbing aerosols in some dust plumes. In contrast to fire plumes, the SSA of

500   dust aerosol showed a clear increasing trend with wavelength. This behavior is likely due to the

501   domination of large particles in dust aerosol, which is in agreement to similar patterns observed in

502   dust source regions *(Dubovik et al., 2002)*. Moreover, an increase of SSA is observed with

503 wavelength for mixed dust-smoke aerosol, suggesting that the aerosol particles were

504 predominantly from dust, albeit mixed with a significant loading of biomass burning.

505

		SSA(450)	SSA(550)	SSA(660)	MEE(450)	MEE(550)	MEE(660)	g(450)	g(550)	g(660)	SAE
Mineral dust	median	0.88	0.90	0.93	0.74	0.68	0.66	0.74	0.72	0.69	-0.35
	3th	0.82	0.82	0.86	0.38	0.38	0.39	0.69	0.67	0.65	-0.56
	25th	0.85	0.87	0.90	0.43	0.43	0.43	0.73	0.72	0.67	-0.48
	75th	0.91	0.93	0.96	0.94	0.85	0.85	0.75	0.74	0.72	-0.25
	97th	0.92	0.95	0.97	1.57	1.37	1.21	0.78	0.76	0.72	-0.12
Biomass burning	median	0.74	0.76	0.72	1.91	1.62	1.34	0.69	0.68	0.61	1.07
	3th	0.70	0.72	0.66	0.94	1.45	1.22	0.64	0.65	0.59	0.59
	25th	0.70	0.76	0.71	1.67	1.48	1.27	0.69	0.65	0.60	0.83
	75th	0.77	0.77	0.74	1.86	1.65	1.55	0.72	0.68	0.62	1.15
	97th	0.78	0.77	0.76	2.38	1.92	1.58	0.73	0.68	0.63	1.64
Mixed dust-Biomass burning	median	0.76	0.77	0.81	1.58	1.40	1.30	0.73	0.66	0.64	0.38
	3th	-	-	-	-	-	-	-	-	-	-
	25th	-	-	-	-	-	-	-	-	-	-
	75th	-	-	-	-	-	-	-	-	-	-
	97th	-	-	-	-	-	-	-	-	-	-
Anthropogenic Pollution	median	0.83	0.84	0.85	2.60	2.49	1.90	0.60	0.61	0.62	0.75
	3th	0.78	0.79	0.81	0.70	1.24	0.54	0.60	0.59	0.54	0.30
	25th	0.80	0.82	0.83	2.14	2.25	1.53	0.62	0.60	0.56	0.65
	75th	0.84	0.86	0.85	3.51	2.96	2.53	0.69	0.62	0.67	0.89
	97th	0.87	0.88	0.90	3.70	4.83	2.74	0.73	0.64	0.70	0.94

506
507 **Table 2. Single scattering albedo, mass extinction efficiency (in $m^2\ g^{-1}$), asymmetry parameter**
508 **and scattering Ångstrom exponent for the dominant aerosol classification.**
509
510 As shown in Table 2, the observed variability of *SSA* reflects a large variability for *MEE* at 550nm,

511 which spans a wide range from 0.38 to 1.37 $m^2\ g^{-1}$, 1.45 to 1.92 $m^2\ g^{-1}$ and 1.24 to 4.83 $m^2\ g^{-1}$ for

512 dust, biomass burning for anthropogenic polluted aerosols, respectively. *MEE* is heavily influenced

513 by the mass concentrations in the accumulation mode where the aerosol is optically more efficient

514 in extinguishing radiation. We found *MEE* to be positively correlated with *SAE* (not shown), which

515 was expected because of the dependence of *MEE* on particle size. In contrast, the values of *g*

516 appear to differ only little between the sampled plumes for a given aerosol class. We found *g* in the

517 range of 0.67–0.76 for dust, 0.65–0.68 for biomass burning and 0.59–0.64 for anthropogenic

518 polluted aerosols at 550 nm. *g* values in dust plumes were high, which is expected due to the

519 presence of coarse particles contributing to forward scattering.

520

521   This analysis includes sampled aerosols originating from different source regions and having
522   undergone different aging and mixing processes, which could explain some of the variability. The
523   impact of these factors on the magnitude and spectral dependence of optical parameters will be
524   investigated in the following section.

525

526   **4. Discussion**

527   **4.1. Contribution of local anthropogenic pollution on aerosol absorption properties**

528   Figure 7 shows the vertical distribution of *SSA, SAE* and NO_x mixing ratio for the dominant
529   aerosol classification. We exclusively consider measurements acquired during SLRs, since only
530   during these phases the whole set of aerosol optical properties were measured. In dust plumes, if
531   we exclude the case of mixing with biomass burning aerosol, SSAs were fairly constant above 2.5
532   km amsl with values ranging between 0.90 and 0.93 at 550 nm, in agreement with values reported
533   over dust source regions *(Schladitz et al., 2009; Formenti et al., 2011b; Ryder et al., 2013, 2018)*.
534   Despite the range of sources identified during DACCIWA, dust absorption properties do not seem
535   to be clearly linked to particle origin or time of transport. Aerosols were more absorbing within the
536   low-altitude dust plumes with SSA values dropping to 0.81. *SAE* values exhibited simultaneously a
537   sharp increase close to zero below 2.5 km amsl. This is consistent with a higher concentration of
538   fine particles, though the value of *SAE* was still much lower than for pollution or background
539   aerosol (i.e. where it is typically > 0.2), which means that scattering was still dominated by larger
540   particles. Based on the whole sets of observations, the strong variation in the light-absorption
541   properties of dust-dominated aerosol over SWA could be attributed to the degree of mixing into the
542   vertical column with either freshly emitted aerosols from urban/industrial sources or long-range
543   transported biomass burning aerosol.

544

545   One of the critical factors in the calculation of aerosol direct and semi-direct radiative effects is the
546   mixing state of the aerosols, which can significantly affect absorbing properties. There were no
547   direct observational constraints available on this property during the DACCIWA airborne
548   campaign. However, we investigated the probable aerosol mixing state by calculating composite
549   SSA from the aerosol size distribution. On the basis of Figure 5, dust size distributions showed
550   only minor discrepancies in the mean and standard deviation of the coarse mode but significant
551   differences in the balance between fine and coarse modes, which suggests low internal mixing of
552   dust with other atmospheric species. The size distributions of mixed dust-pollution have been
553   deconvoluted by weighting the size distributions of mineral dust and anthropogenic pollution
554   aerosol averaged over the respective flights. This assumes that dust was externally mixed with the

555   anthropogenic pollution particles and assumes a homogeneous size distribution for the dust and

556   anthropogenic pollution aerosol throughout a flight. σ_{scat} and σ_{abs} were then calculated using Mie

557   theory from each composite size distributions and the corresponding k and m. The refractive

558   indices at 550 nm were assumed to be 1.52-0.002i and 1.60-0.040i for dust and anthropogenic

559   pollution particles, respectively, which are the mean values deduced from the data inversion

560   procedure (i.e. section 2.3.1) throughout the campaign. The resulting σ_{scat} and σ_{abs} were used to

561   calculate a composite *SSA*. A similar calculation was performed for the mixed dust-biomass

562   burning case. Figure 7 shows a good agreement with the observations of *SSA*, implying that

563   external mixing appears to be a reasonable assumption to compute aerosol direct and semi-direct

564   radiative effects in these dust layers for modeling applications. This is consistent with the filter

565   analysis performed during AMMA and SAMUM-2, which did not reveal any evidence of internal

566   mixing in both mixed dust-biomass burning and dust-anthropogenic pollution layers *(Chou et al.,*

567   *2008; Lieke et al., 2011; Petzold et al., 2011)*.

568
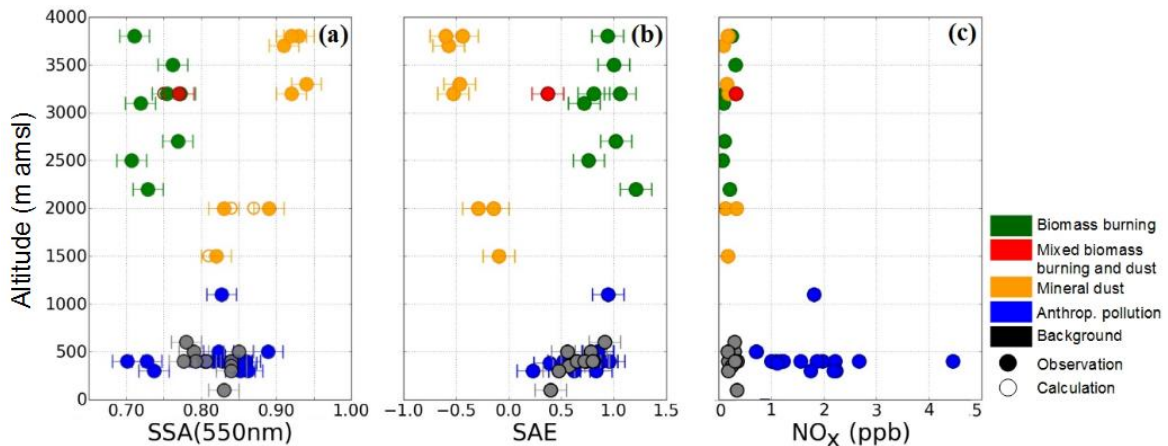
569
570   **Figure 7. Vertical distribution of (a) the single scattering albedo at 550 nm, (b) the scattering**
571   **Ångstrom exponent and (c) NO$_x$ mixing ratio for the dominant aerosol classification. In panel**
572   **(a), full circles represent *SSA* measurements and empty circles represent composite *SSA***
573   **calculated by deconvoluting size distribution measurements in mixed dust layers and**
574   **assuming an external mixing state.**

575
576   *SSA*, *SAE* and NO$_x$ of biomass burning plumes did not significantly vary with height from 2.2 to

577   3.8 km amsl. Moreover, the size distribution of biomass burning aerosols for the observed cases

578   did not show significant contribution of ultrafine particles (Figure 5). These observations seem to

579   indicate that the absorption properties of biomass burning plumes were not affected by direct

580   pollution emissions/

581

582   In the boundary layer, the similar *SSA* and *SAE* in anthropogenic pollution and background plumes

583   suggests that background aerosol may be rather called background pollution originating from a

584   regional background source in the far field. Our analysis of the spectral dependence of *SSA*

585   showed no apparent signature of anthropogenic pollution aerosols (see section 3.3) despite a strong

586   increase of aerosol number concentrations in air masses crossing urban centers (see section 3.2).

587   This can be explained by two factors: First, the majority of accumulation mode particles were

588   present in the background, while the large proportion of aerosols emitted from cities resided in the

589   ultrafine mode particles that have less scattering efficiencies (Figure 5). Second, large amounts of

590   absorbing aerosols in the background can minimize the impact of further increase of absorbing

591   particles to the aerosol load. The high CO values (~180 ppb) observed in background conditions

592   further indicates a strong contribution of combustion emissions at the surface. Recent studies

593   showed a large background of biomass burning transported from the Southern Hemisphere in SWA

594   that dominated the aerosol chemical composition in the boundary layer *(Menut et al., 2018;*

595   *Haslett et al., 2019)*. The high absorbing properties (*SSA*~0.81 at 550nm) and the presence of

596   particles both in the accumulation and super-micron modes (i.e. section 3.2.) in background

597   plumes are consistent with being a mixture of aged absorbing biomass burning and Atlantic marine

598   aerosol. These results highlight that aerosol optical properties at the surface were dominated by the

599   widespread biomass burning particles at regional scale.

600

4.2. Aging as a driver for absorption enhancement of biomass burning aerosol

602   The optical properties of aerosols are determined by either the aerosol chemical composition, the

603   aerosol size distribution, or both. Changes in the size distribution of biomass burning aerosol due

604   to coagulation and condensation have been shown to alter the *SSA*, as particles increase towards

605   sizes for which scattering is more efficient *(Laing et al., 2016)*. Variations in particle chemical

606   composition, caused by source emissions and aging processes associated with gas-to-particle

607   transformation and internal mixing, has been shown to change the *SSA (Abel et al., 2003; Petzold*

608   *et al., 2011)*.

609

610   In order to determine the contributions from size distribution and chemical composition to the

611   variation of *SSA* in biomass burning plumes, *SSA* is presented as a function of *SAE* and *k* in Figure

612   7a and b, respectively. *k* was iteratively varied to reproduce the experimental scattering and

613   absorption coefficients, as described in section 2.3.1. It appears that the variation of the size

614   distribution (assessed via *SAE* in Figure 8a) had minimal impact in determining the variability of

615   *SSA*. Thus, the observations suggest that there was no effect of plume age on the size distribution,

616   consistent with previous observations of size distribution in aged North American biomass
617   burning plumes *(Sakamoto et al., 2015; Carrico et al., 2016; Laing et al., 2016)*. Using a
618   Lagrangian microphysical model, *Sakamoto et al. (2015)* have shown a rapid shift to larger sizes
619   for biomass burning plumes within the first hours of aging. Less drastic but similarly rapid growth
620   by coagulation was seen by *Capes et al. (2008)* in their box model. Given that the biomass burning
621   plumes sampled during DACCIWA had more than 5 days in age, the quick size-distribution
622   evolution within the early plume stages might explain the limited impact of the size distribution on
623   the *SSA*.
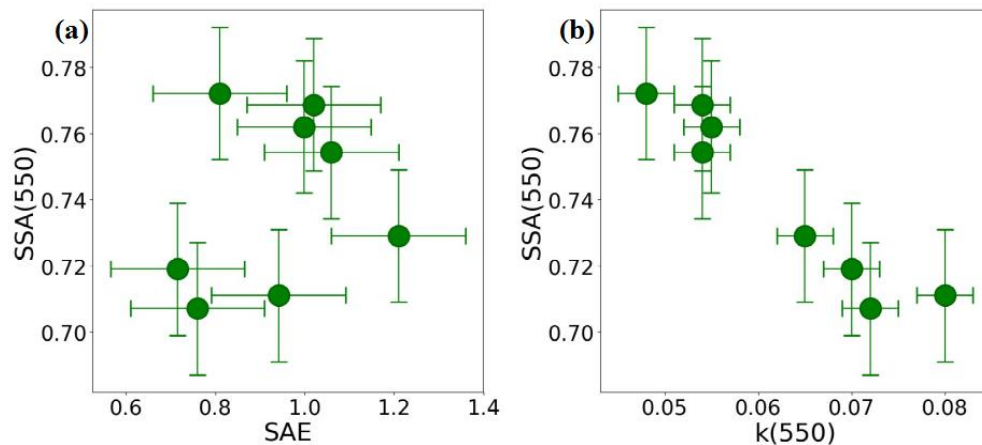
624
625   **Figure 8. Contribution to single scattering albedo (a) from particle size (assessed via *SAE*)**
626   **and (b) from composition (assessed via *k*) in biomass burning plumes.**
627

628   In contrast, Figure 8b shows that there was a consistent decrease in *SSA* with increasing *k,*
629   although there is some variability between the results from different plumes. The observed
630   variability of *SSA* is reflected in a large variability of *k*, which is estimated to span the large range
631   0.048–0.080 at 550 nm. k depends both on the aerosol chemical composition and size distribution
632   *(Mita and Isono, 1980).* Given that *SSA* was found to be independent of the aerosol size
633   distribution (Figure 8a), Figure 8b suggests that *SSA* variability was strongly influenced by the
634   variability in composition of biomass burning aerosol, implying a high contribution for light-
635   absorbing particles. No clear tendency was found for the wavelength dependence of *k*, which in
636   some of the cases increases with wavelength and in others decreases (not shown). In field
637   observation, significant absorption and strong spectral dependence (values of AAE >1.7) in
638   biomass burning plumes have been frequently attributed to the presence of brown carbon (BrC)
639   [Kirchstetter et al., 2004; Sandradewi et al., 2008; Romonosky et al., 2019; Chakrabarty et al.,

640   2010; Pokhrel et al., 2016]. Contrary to the current understanding, our measurements show that the

641   contribution of BrC to light absorption is negligible as AAE values ranged from 0.9 to 1.1 with a

642   median value of 1.0. (Figure 2B). Theoretically, fine-mode aerosol with absorption determined

643   exclusively by BC would have AAE equal to 1.0, since BC is expected to have a spectrally

644   constant k (Bond et al., *2013)*. Therefore, the low *SSA* values observed in biomass burning plumes

645   over SWA and the small spectral variation of *k* both suggest that BC is the dominant absorber in

646   the visible and near-IR wavelengths for these biomass burning aerosols.

647

648   Compared with past in-situ measurements of aged biomass burning aerosol, *SSA* values over SWA

649   (0.71–0.77 at 550 nm) are at the lower end of those reported worldwide (0.73–0.99 at 550 nm)

650   (*Maggi et al., 2003; Reid et al. 2005; Johnson et al., 2008; Corr et al. 2012; Laing et al. 2016)*.

651   This can be attributed in part to the high flaming versus smoldering conditions of African smoke

652   producing more BC particles *(Andreae and Merlet, 2001; Reid et al., 2005)*, which inherently have

653   low *SSA* compared to other regions *(Dubovick et al*. 2002). However, *SSA* values over SWA are

654   significantly lower than the range reported near emission sources in sub-Saharan Africa and over

655   the southeast Atlantic, where values span over 0.84–0.90 at 550 nm *(Haywood et al., 2003b;*

656   *Pistone et al., 2019)*. Recent observations carried out on Ascension Island to the south-west of the

657   DACCIWA region showed that smoke transported from Central and South African fires can be

658   very light absorbing over the July-November burning season but *SSA* values were still higher

659   (0.80±0.02 at 530 nm; *Zuidema et al., 2018*) than those reported over SWA. A possible cause of

660   the lower *SSA* in SWA is that Ascension Island is much closer to the local sources and the aerosol

661   is therefore less aged.

662

663   Currently there are few field measurements of well-aged biomass burning emissions. Our

664   knowledge of biomass burning aerosol primarily comes from laboratory experiments and near-

665   field measurements taken within a few hours of a wildfire *(Abel et al., 2003; Yokelson et al., 2009;*

666   *Adler et al., 2011; Haywood et al., 2003b; Vakkari et al., 2014; Zhong and Jang, 2014; Forrister*

667   *et al., 2015; Laing et al., 2016; Zuidema et al., 2018*). Exception made of the study by *Zuidema et*

668   *al. (2018)* over the southeast Atlantic, it is generally found that the aged biomass burning aerosol

669   particles are less absorbing than freshly emitted aerosols due to a combination of condensation of

670   secondary organic species and an additional increase in size by coagulation. This is in contrasts to

671   our results showing that *SSA* of biomass burning aerosols were significantly lower than directly

672   after emission and that the evolution of *SSA* occurred long time after emission.

673

674   There are three possible explanations for these results. First, one must consider sample bias. As
675   regional smoke ages, it can be enriched by smoke from other fires that can smolder for days
676   producing large quantities of non-absorbing particles, thereby increasing the mean *SSA (Reid et al.,*
677   *2005; Laing et al., 2016)*. However, during DACCIWA, biomass burning plumes were transported
678   over the Atlantic Ocean and were probably less influenced by multiple fire emissions. Second,
679   there is evidence that fresh BC particles become coated with sulfate and organic species as the
680   plume ages in a manner that enhances their light absorption *(Lack et al., 2012; Schwarz et al.,*
681   *2008)*. Finally, organic particles produced during the combustion phase can be lost during the
682   transport through photobleaching, volatilization and/or cloud-phase reactions *(Clarke et al., 2007;*
683   *Lewis et al., 2008; Forrister et al., 2015)*, which is consistent with the low *SSA* and *AAE* values we
684   observed. Assessing whether these aging processes impact the chemical components and
685   henceforth optical properties of transported biomass burning aerosol would need extensive
686   investigation of aerosol chemical composition that will be carried out in a subsequent paper.
687

5. Conclusions

689   This paper provides an overview of *in-situ* airborne measurements of vertically resolved aerosol
690   optical properties carried out over SWA during the DACCIWA field campaign in June-July 2016.
691   The peculiar dynamics of the region lead to a chemically complex situation, which enabled
692   sampling various air masses, including long-range transport of biomass burning from Central
693   Africa and dust from Sahelian and Saharan sources, local anthropogenic plumes from the major
694   coastal cities, and mixtures of these different plumes. This work fills a research gap by providing,
695   firstly, key climate relevant aerosol properties *(SSA, MEE, g, SAE, AAE)* and secondly,
696   observations of the impact of aging and mixing processes on aerosols optical properties.
697

698   The aerosol vertical structure was very variable and mostly influenced by the origin of air mass
699   trajectories. While aerosol extinction coefficients generally decreased with height, there were
700   distinct patterns of profiles during dust and biomass burning transport to SWA. When present,
701   enhanced values of extinction coefficient up to 240 Mm^{-1} were observed in the 2–5 km amsl range.
702   These elevated aerosol layers were dominated by either dust or biomass burning aerosols, which is
703   consistent with what would be expected on the basis of the atmospheric circulations during the
704   monsoon season *(McConnell et al., 2008; Knippertz et al., 2017)*. However, during one flight a
705   mixture of dust and biomass burning was found in a layer at around 3 km amsl, implying that there
706   may be substantial variability in the idealized picture. In the lower troposphere, the large
707   anthropogenic pollution plumes extended as far as hundreds of kilometers from the cities emission

708   sources and were not limited to the boundary layer but occurred also at higher levels up to 2.5 km

709   amsl, which is explained by vertical transport and mixing processes, partly triggered by the

710   orography of SWA (*Deroubaix et al., 2019; Flamant et al., 2018a*). The analysis of the aerosol size

711   distributions, *SAE* and NO_x suggests a strong mixing of dust with anthropogenic pollution particles

712   in dust layers transported below 2.5 km amsl, whereas biomass burning plumes that were

713   transported more northward were not affected by this mixing. Both transport pathways and vertical

714   structures of biomass burning and dust plumes over SWA appear to be the main factors affecting

715   the mixing of anthropogenic pollution with dust and biomass burning particles.

716

717   The aerosol light absorption in dust plumes was strongly enhanced as the result of this mixing. We

718   find a decrease of *SSA(550nm)* from 0.92 to 0.81 for dust affected by anthropogenic pollution

719   mixing compared to the situation in which the dust plumes moved at higher altitudes across SWA.

720   Comparison of the particle size distributions of the different dust plumes showed a large

721   contribution of externally mixed fine mode particles in mixed layers, while there was no evidence

722   for internal mixing of coarse particles. Concurrent optical calculations by deconvoluting size

723   distribution measurements in mixed layers and assuming an external mixing state allowed to

724   reproduce the observed *SSA*s. This implies that an external mixing would be a reasonable

725   assumption to compute aerosol direct and semi-direct radiative effects in mixed dust layers.

726

727   Despite a strong increase of aerosol number concentration in air masses crossing urban

728   conglomerations, the magnitude of the spectral *SSA*s was comparable to the background.

729   Enhancements of light absorption properties were seen in some pollution plumes, but were not

730   statistically significant. A persistent spectral signature of biomass burning aerosols in both

731   background and pollution plumes highlights that the aerosol optical properties in the boundary

732   layer were strongly affected by the ubiquitous biomass burning aerosols transported from Central

733   Africa *(Menut et al., 2018; Haslett et al., 2019)*. The large proportion of aerosols emitted from the

734   cities of Lomé, Accra and Abidjan that resided in the ultrafine mode particles have limited impact

735   on already elevated amounts of accumulation mode particles having a maximal absorption

736   efficiency. As a result, in the boundary layer, the contribution from local city emissions to aerosol

737   optical properties were of secondary importance at regional scale compared with this large

738   absorbing aerosol mass. While local anthropogenic emissions are expected to rise as SWA is

739   currently experiencing major economic and population growth, there is increasing evidence that

740   climate change is increasing the frequency and distribution of fire events *(Joly et al., 2015)*. In

741   terms of future climate scenarios and accompanying aerosol radiative forcing, whether the large

742   biomass burning events that occur during the monsoon season would limit the radiative impact of

743   increasing anthropogenic emissions, remains an open and important question.

744

745   The *SSA* values of biomass burning aerosols transported in the free troposphere were very low

746   (0.71–0.77 at 550 nm) and have only rarely been observed in the atmosphere. The variability in

747   *SSA* was mainly controlled by the variability in aerosol composition (assessed via *k*) rather than by

748   variations in the aerosol size distribution. Correspondingly, values of *AAE* ranged from 0.9 to 1.1,

749   suggesting that BC particles were the dominant absorber in the visible for these biomass burning

750   aerosols. In recent years the southern Atlantic Ocean, especially the area of the west coast of

751   Africa, became an increasing focus in the research community, through the ORACLES/LASIC

752   (ObseRvations of Aerosols above CLouds and their intEractionS/Layered Atlantic Smoke

753   Interactions with Clouds), AEROCLO-sA (AErosol RadiatiOn and CLOuds in Southern Africa –

754   AEROCLO-SA) and CLARIFY (Cloud and Aerosols Radiative Impact and Forcing) projects

755   *(Zuidema et al.; 2016; Zuidema et al.; 2018; Formenti et al.; 2019)*. Comparison with literature

756   showed a consistent picture of increasing absorption enhancement of biomass burning aerosol

757   from emission to remote locations. Further, the range of *SSA* values over SWA was slightly lower

758   than that reported on Ascension Island to the south-west of the DACCIWA region, which

759   underscores that the evolution of *SSA* occurred long time after emission. While the mechanism

760   responsible for this phenomenon warrants further study, our results support the growing body of

761   evidence that the optical parameters used in regional/global climate modeling studies, especially

762   absorption by biomass burning aerosols, have to be better constrained using these recent

763   observations to determine the direct and semi-direct radiative effects of smoke particles over this

764   region *(Mallet et al. 2019)*. In particular and regarding the very high absorbing properties of

765   smoke, specific attention should be dedicated to the semi-direct effect of biomass burning aerosols

766   at the regional scale and its relative contribution to the indirect radiative effect.

767

768   We believe the set of DACCIWA observations presented here is representative of the regional

769   mean and variability in aerosol optical properties that can be observed during the monsoon season

770   over SWA, as the main dynamical features were in line with climatology *(Knippertz et al., 2017)*.

771   This is why results from the present study will serve as input and constraints for climate modeling

772   to better understand the impact of aerosol particles on the radiative balance and cloud properties

773   over this region and also will substantially support remote sensing retrievals.

774 *Data availability.*

775 All data used in this study are publicly available on the AERIS Data and Service Center, which can

776 be found at http://baobab.sedoo.fr/DACCIWA.

777

778 *Author contributions.*

779 CD conducted the analysis of the data and wrote the paper. CD, TB, FB, NM, AC, PD, JB, RD, KS

780 and AS operated aircraft instruments and processed and/or quality-controlled data. MM provided

781 expertise on aerosol-climate interaction processes. CF and PK were PIs, who led the funding

782 application and coordinated the DACCIWA field campaign. All co-authors contributed to the

783 writing of the paper.

784

785 *Acknowledgements.*

786 The research leading to these results has received funding from the European Union 7th

787 Framework Programme (FP7/2007-2013) under Grant Agreement no. 603502 (EU project

788 DACCIWA: Dynamics-aerosol-chemistry-cloud interactions in West Africa). The European

789 Facility for Airborne Research (EUFAR, http://www.eufar.net/) also supported the project through

790 the funding of the Transnational Activity project OLACTA and MICWA. We thank the Service des

791 Avions Français Instrumentés pour la Recherche en Environnement (SAFIRE, a joint entity of

792 CNRS, Météo-France, and CNES) and operator of the ATR-42 for their support during the aircraft

793 campaign. Cyrielle Denjean thanks CNES for financial support. The authors would like to thank

794 Bruno Piguet (CNRM) and Michel Ramonet (LSCE) for their support in the data processing.

795 **Appendix 1. Summary of flight information. All flights were conducted during 2016.**

Flight number	Date	Take off time (UTC)	Landing time (UTC)	Events observed
F17	29 June	14:17	17:10	Export of pollution from Lomé
F18	30 June	12:52	16:29	Export of pollution from Lomé
F19	1 July	10:35	14:06	Export of pollution from Accra
F20	2 July	09:53	13:21	Export of pollution from Lomé Dust outbreak
F21	2 July	15:04	18:29	Export of pollution from Lomé Biomass burning outbreak Mixed dust-biomass burning outbreak
F22	3 July	09:54	13:29	Export of pollution from Lomé
F24	6 July	07:17	11:03	Export of pollution from Abidjan
F27	8 July	05:52	09:28	Export of pollution from Accra
F28	8 July	10:53	14:22	Dust outbreak
F29	10 July	10:31	14:11	Export of pollution from Lomé Dust outbreak
F30	11 July	07:19	11:01	Export of pollution from Abidjan Biomass burning outbreak
F31	11 July	13:48	16:42	Biomass burning outbreak
F32	12 July	13:56	17:20	Export of pollution from Accra
F33	13 July	12:40	16:11	Biomass burning outbreak
F35	15 July	09:32	13:00	Export of pollution from Lomé

796

797 **Appendix 2. Data inversion procedure to calculate the aerosol microphysical and optical**

798 **parameters.**

799
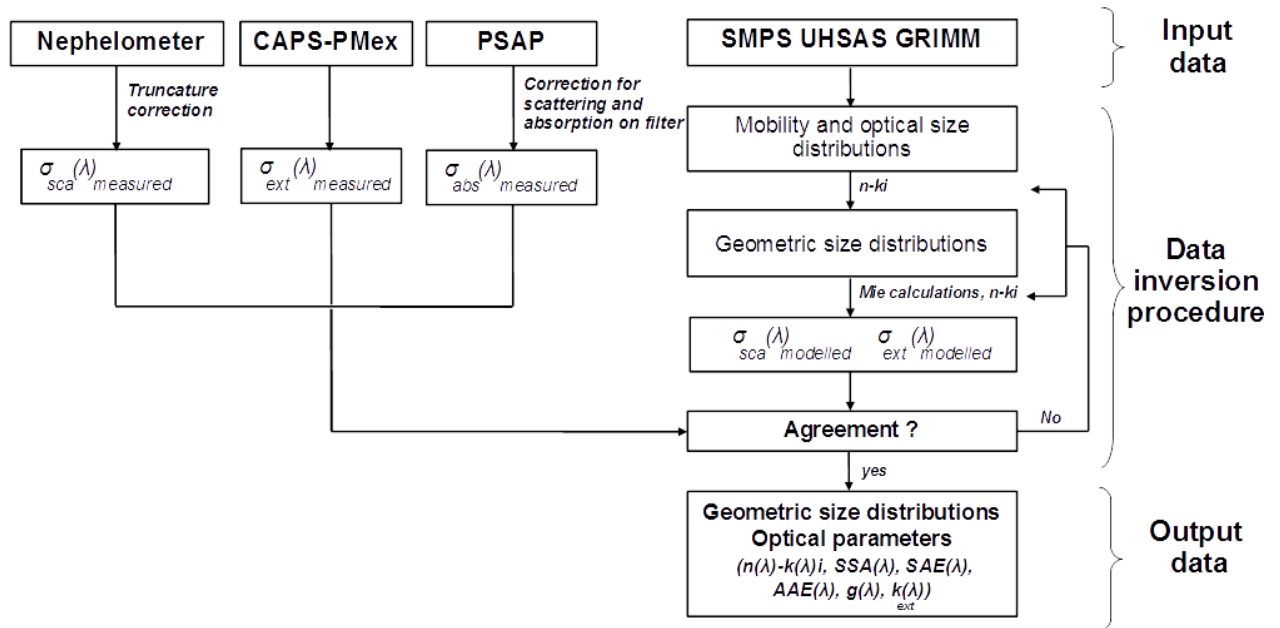
References

800   **References**

801   Abel, S. J., Haywood, J. M., Highwood, E. J., Li, J., and Buseck,P. R.: Evolution of biomass

802   burning aerosol properties from anagricultural fire in southern Africa, Geophys. Res. Lett., 30,

803   1783, doi:10.1029/2002GL017342, 2003.

804   Adler, G., Flores, J. M., Abo Riziq, A., Borrmann, S., and Rudich, Y., Chemical, physical, and

805   optical evolution of biomass burning aerosols: a case study, Atmos. Chem. Phys., 11, 1491-

806   1503, https://doi.org/10.5194/acp-11-1491-2011, 2011.

807   Andreae, M.O. and Merlet, P., Emission of Trace Gases and Aerosols from Biomass Burning.

808   Global Biogeochemical Cycles, 15, 955-966 , 2001.

809   Ansmann, A., Petzold, A., Kandler, K., Tegen, I. N. A., Wendisch, M., Müller, D., Weinzierl, B.,

810   Müller, T., and Heintzenberg, J.: Saharan Mineral Dust Experiments SAMUM–1 and

811   SAMUM–2: what have we learned?, Tellus B, 63, 403-429, doi: 10.1111/j.1600-

812   0889.2011.00555.x, 2011.

813   Bond, T. C., Doherty, S. J., Fahey, D. W., Forster, P. M., Berntsen,T., DeAngelo, B. J., Flanner, M.

814   G., Ghan, S., Kärcher, B., Koch,D., Kinne, S., Kondo, Y., Quinn, P. K., Sarofim, M. C.,

815   Schultz,M. G., Schulz, M.,Venkataraman, C., Zhang, H., Zhang, S., Bellouin,N., Guttikunda, S.

816   K., Hopke, P. K., Jacobson, M. Z.,Kaiser, J. W., Klimont, Z., Lohmann, U., Schwarz, J. P.,

817   Shindell,D., Storelvmo, T., Warren, S. G., and Zender, C. S.: Bounding the role of black carbon

818   in the climate system: A scientific assessment, J. Geophys. Res., 118, 1–173,

819   doi:10.1002/jgrd.50171, 2013.

820   Boucher, O., D. Randall, P. Artaxo, C. Bretherton, G. Feingold, P. Forster, V.-M. Kerminen, Y.

821   Kondo, H. Liao, U. Lohmann, P. Rasch, S.K. Satheesh, S. Sherwood, B. Stevens, and X.Y.

822   Zhang: Clouds and aerosols. In Climate Change 2013: The Physical Science Basis.

823   Contribution of Working Group I to the Fifth Assessment Report of the Intergovernmental

824   Panel on Climate Change. T.F. Stocker, D. Qin, G.-K. Plattner, M. Tignor, S.K. Allen, J.

825   Doschung, A. Nauels, Y. Xia, V. Bex, and P.M. Midgley, Eds. Cambridge University Press, pp.

826   571-657, doi:10.1017/CBO9781107415324.016, 2013.

827   Capes, G., B. Johnson, G. McFiggans, P. I. Williams, J. M. Haywood, and H. Coe, Aging of

828   biomass burning aerosols over West Africa: Aircraft measurements of chemical composition,

829   microphysical properties and emission ratios, J. Geophys. Res., 113, D00C15,

830   doi:10.1029/2008JD009845, 2008.

831   Carrico, C.M., Prenni, A.J., Kreidenweis, S.M., Levin, E.J., McCluskey, C.S., DeMott, P.J.,

832   McMeeking, G.R., Rapidly evolving ultrafine and fine mode biomass smoke physical

833   properties: comparing laboratory and field results, J. Geophys. Res. Atmos., 121(10),
834   10.1002/2015JD024389, 2016.

835   Chakrabarty, R. K., Moosmüller, H., Chen, L.-W. A., Lewis, K., Arnott, W. P., Mazzoleni, C.,
836   Dubey, M. K., Wold, C. E., Hao, W. M., and Kreidenweis, S. M.: Brown carbon in tar balls
837   from smoldering biomass combustion, Atmos. Chem. Phys., 10, 6363–6370,
838   https://doi.org/10.5194/acp-10-6363-2010, 2010.

839   Chen, G., Ziemba, L. D., Chu, D. A., Thornhill, K. L., Schuster, G. L., Winstead, E. L., Diskin, G.
840   S., Ferrare, R. A., Burton, S. P., Ismail, S., Kooi, S. A., Omar, A. H., Slusher, D. L., Kleb, M.
841   M., Reid, J. S., Twohy, C. H., Zhang, H., and Anderson, B. E.: Observations of Saharan dust
842   microphysical and optical properties from the Eastern Atlantic during NAMMA airborne field
843   campaign, Atmos. Chem. Phys., 11, 723-740, https://doi.org/10.5194/acp-11-723-2011, 2011.

844   Chou, C., P. Formenti, M. Maille, P. Ausset, G. Helas, S. Osborne, and M. Harrison, Size
845   distribution, shape and composition of dust aerosols collected during the AMMA SOP0 field
846   campaign in the northeast of Niger, January 2006, J. Geophys. Res., 113, D00C10,
847   doi:10.1029/2008JD009897, 2008.

848   Clarke, A., McNaughton, C., Kapustin, V., Shinozuka, Y., Howell, S., Dibb, J., Zhou, J., Anderson,
849   B., Brekhovskikh, V., Turner, H., and Pinkerton, M.: Biomass burning and pollution aerosol
850   over North America: organic components and their influence on spectral optical properties and
851   humidification response, J. Geophys. Res., 112, D12S18, doi:10.1029/2006JD007777, 2007.

852   Corr, C. A., Hall, S. R., Ullmann, K., Anderson, B. E., Beyersdorf, A. J., Thornhill, K. L., Cubison,
853   M. J., Jimenez, J. L., Wisthaler, A., and Dibb, J. E.: Spectral absorption of biomass burning
854   aerosol determined from retrieved single scattering albedo during ARCTAS, Atmos. Chem.
855   Phys., 12, 10505-10518, https://doi.org/10.5194/acp-12-10505-2012, 2012.

856   Deetz, K., Vogel, H., Haslett, S., Knippertz, P., Coe, H., and Vogel, B.: Aerosol liquid water
857   content in the moist southern West African monsoon layer and its radiative impact, Atmos.
858   Chem. Phys., 18, 14271-14295, https://doi.org/10.5194/acp-18-14271-2018, 2018.

859   Denjean, C., Cassola, F., Mazzino, A., Triquet, S., Chevaillier, S., Grand, N., Bourrianne, T.,
860   Momboisse, G., Sellegri, K., Schwarzenbock, A., Freney, E., Mallet, M., and Formenti, P.: Size
861   distribution and optical properties of mineral dust aerosols transported in the western
862   Mediterranean, Atmos. Chem. Phys., 16, 1081-1104, https://doi.org/10.5194/acp-16-1081-2016,
863   2016.

864   Deroubaix, A., Menut, L., Flamant, C., Brito, J., Denjean, C., Dreiling, V., Fink, A., Jambert, C.,
865   Kalthoff, N., Knippertz, P., Ladkin, R., Mailler, S., Maranan, M., Pacifico, F., Piguet, B., Siour,
866   G., and Turquety, S.: Diurnal cycle of coastal anthropogenic pollutant transport over southern

West Africa during the DACCIWA campaign, Atmos. Chem. Phys., 19, 473-497, https://doi.org/10.5194/acp-19-473-2019, 2019.

Di Biagio, C., Formenti, P., Doppler, L., Gaimoz, C., Grand, N., Ancellet, G., Attié, J.-L., Bucci, S., Dubuisson, P., Fierli, F., Mallet, M., and Ravetta, F.: Continental pollution in the Western Mediterranean basin: large variability of the aerosol single scattering albedo and influence on the direct shortwave radiative effect, Atmos. Chem. Phys., 16, 10591-10607, https://doi.org/10.5194/acp-16-10591-2016, 2016.

Dubovik, O., Holben, B. N., Eck, T. F., Smirnov, A., Kaufman, Y. J., King, M. D., Tanre, D.,and Slutsker, I.: Climatology of atmospheric aerosol absorption and optical properties in key locations, J. Atmos. Sci., 59, 590–608, 2002.

Flamant, C., Deroubaix, A., Chazette, P., Brito, J., Gaetani, M., Knippertz, P., Fink, A. H., de Coetlogon, G., Menut,L., Colomb, A., Denjean, C., Meynadier, R., Rosenberg, P., Dupuy, R., Dominutti, P., Duplissy, J., Bourrianne,T., Schwarzenboeck, A., Ramonet, M., and Totems, J.: Aerosol distribution in the northern Gulf of Guinea: local anthropogenic sources, long-range transport, and the role of coastal shallow circulations, Atmospheric Chemistryand Physics, 18, 12 363–12 389, https://doi.org/10.5194/acp-18-12363-2018, 2018a.

Flamant C., Knippertz, P., Fink, A. H., Akpo, A., Brooks, B., Chiu, C. J., Coe, H., Danuor, S., Evans, M., Jegede, O., Kalthoff, N., Konaré, A., Liousse, C., Lohou, F., Mari, C., Schlager, H., Schwarzenboeck, A., Adler, B., Amekudzi, L., Aryee, J., Ayoola, M., Batenburg, A. M., Bessardon, G., Borrmann, S., Brito, J., Bower, K., Burnet, F., Catoire, V., Colomb, A., Denjean, C., Fosu-Amankwah, K., Hill, P. G., Lee, J., Lothon, M., Maranan, M., Marsham, J., Meynadier, R., Ngamini, J.-B., Rosenberg, P., Sauer, D., Smith, V., Stratmann, G, Taylor, J. W., Voigt, C., and Yoboué, V.: The Dynamics-Aerosol-Chemistry-Cloud Interactions in West Africa field campaign: Overview and research highlights, B. Am. Meteorol. Soc., 99, 83–104, https://doi.org/10.1175/BAMS-D-16-0256.1, 2018b.

Formenti, P., Schütz, L., Balkanski, Y., Desboeufs, K., Ebert, M., Kandler, K., Petzold, A., Scheuvens, D., Weinbruch, S., and Zhang, D.: Recent progress in understanding physical and chemical properties of African and Asian mineral dust, Atmos. Chem. Phys., 11, 8231–8256, https://doi.org/10.5194/acp-11-8231-2011, 2011a.

Formenti, P., Rajot, J. L., Desboeufs, K., Saïd, F., Grand, N.,Chevaillier, S., and Schmechtig, C.: Airborne observations of mineral dust over western Africa in the summer Monsoons eason: spatial and vertical variability of physico-chemical and optical properties, Atmos. Chem. Phys., 11, 6387–6410,doi:10.5194/acp-11-6387-2011, 2011b.

Formenti, P., B. D'Anna, C. Flamant, M. Mallet, S.J. Piketh, K. Schepanski, F. Waquet, F. Auriol, G. Brogniez, F. Burnet, J. Chaboureau, A. Chauvigné, P. Chazette, C. Denjean, K. Desboeufs, J. Doussin, N. Elguindi, S. Feuerstein, M. Gaetani, C. Giorio, D. Klopper, M.D. Mallet, P. Nabat, A. Monod, F. Solmon, A. Namwoonde, C. Chikwililwa, R. Mushi, E.J. Welton, and B. Holben, 0: The Aerosols, Radiation and Clouds in southern Africa (AEROCLO-sA) field campaign in Namibia: overview, illustrative observations and way forward. *Bull. Amer. Meteor. Soc.,* 0, https://doi.org/10.1175/BAMS-D-17-0278.1, 2019.

Forrister, H., Liu, J., Scheuer, E., Dibb, J., Ziemba, L., Thornhill, K. L., Anderson, B., Diskin, G., Perring, A. E., and Schwarz, J. P.: Evolution of brown carbon in wildfire plumes, Geophys. Res. Lett., 42, 4623–4630, 2015.

Haslett, S. L., Taylor, J. W., Evans, M., Morris, E., Vogel, B., Dajuma, A., Brito, J., Batenburg, A. M., Borrmann, S., Schneider, J., Schulz, C., Denjean, C., Bourrianne, T., Knippertz, P., Dupuy, R., Schwarzenböck, A., Sauer, D., Flamant, C., Dorsey, J., Crawford, I., and Coe, H.: Remote biomass burning dominates southern West African air pollution during the monsoon, Atmos. Chem. Phys. Discuss., https://doi.org/10.5194/acp-2019-38, in review, 2019.

Haywood, J. M., Francis, P., Osborne, S., Glew, M., Loeb, N.,Highwood, E., Tanre, D., Myhre, G., Formenti, P., and Hirst,E.: Radiative properties and direct radiative effect of Saharan dust measured by the C-130 aircraft during SHADE:1. Solar spectrum, J. Geophys. Res.-Atmos., 108, 8577, https://doi.org/10.1029/2002jd002687, 2003a.

Haywood, J. M., S. R. Osborne, P. N. Francis, A. Keil, P. Formenti, M. O.Andreae, and P. H. Kaye, The mean physical and optical properties of regional haze dominated by biomass burning aerosol measured from the C-130 aircraft during SAFARI 2000, J. Geophys. Res., 108(D13), 8473, doi:10.1029/2002JD002226, 2003b.

Haywood, J. M., Pelon, J., Formenti, P., Bharmal, N., Brooks, M., et al.: Overview of the dust and biomass-burning experiment and African Monsoon multidisciplinary analysis special observing period-0., J. Geophys. Res., 113, doi:10.1029/2008JD010077, 2008.

Heintzenberg, J., The SAMUM-1 experiment over Southern Morocco: Overview and introduction, Tellus Ser. B, 61, 2-11, 2009.

Hess, M., Koepke, P., Schult I., Optical properties of aerosols and clouds, Bull. Amer. Meteor. Soc., 79, 831-844, 1998.

Janhäll, S., Andreae, M. O., and Pöschl, U.: Biomass burning aerosol emissions from vegetation fires: particle number and mass emission factors and size distributions, Atmos. Chem. Phys., 10, 1427-1439, https://doi.org/10.5194/acp-10-1427-2010, 2010.

933   Johnson, B. T., Heese, B., McFarlane, S. A., Chazette, P., Jones, A. et al.: Vertical distribution and

934   radiative effects of mineral dust and biomass burning aerosol over West Africa during DABEX,

935   J. Geophys. Res., 113(D17), D00C12, doi:10.1029/2008JD009848,2008.

936   Jolly, W. M., Cochrane, M. A., Freeborn, P. H., Holden, Z. A., Brown, T. J., Williamson, G. J., and

937   Bowman, D. M. J. S.: Climate-induced variations in global wild- fire danger from 1979 to

938   2013, Nat. Commun., 6, 7537, https://doi.org/10.1038/ncomms8537, 2015.

939   Kalthoff, N., Lohou, F., Brooks, B., Jegede, G., Adler, B., Babić, K., Dione, C., Ajao, A.,

940   Amekudzi, L. K., Aryee, J. N. A., Ayoola, M., Bessardon, G., Danuor, S. K., Handwerker, J.,

941   Kohler, M., Lothon, M., Pedruzo-Bagazgoitia, X., Smith, V., Sunmonu, L., Wieser, A., Fink, A.

942   H., and Knippertz, P.: An overview of the diurnal cycle of the atmospheric boundary layer

943   during the West African monsoon season: results from the 2016 observational campaign,

944   Atmos. Chem. Phys., 18, 2913-2928, https://doi.org/10.5194/acp-18-2913-2018, 2018.

945   Kirchstetter T. W. , Novakov, T., and Hobbs, P.: Evidence that the spectral dependence of light

946   absorption by aerosols is affected by organic carbon, J. Geophys. Res., 109,

947   D21208,doi:10.1029/2004JD004999, 2004.

948   Knippertz, P., Evans, M. J., Field, P. R., Fink, A. H., Liousse, C., and Marsham, J. H.: The possible

949   role of local air pollution in climate change in West Africa, Nat. Clim. Change, 5, 815–822,

950   https://doi.org/10.1038/nclimate2727, 2015a.

951   Knippertz, P., Coe, H., Chiu, J. C., Evans, M. J., Fink, A. H., Kalthoff, N., Liousse, C., Mari, C.,

952   Allan, R. P., Brooks, B., Danour, S., Flamant, C., Jegede, O. O., Lohou, F., and Marsham, J. H.:

953   The dacciwa project: Dynamics-Aerosol- Chemistry-Cloud Interactions in West Africa, Bulletin

954   of the American Meteorological Society, 96, 1451–1460, https://doi.org/10.1175/BAMS-D-14-

955   00108.1, http://journals.ametsoc.org/doi/10.1175/BAMS-D-14-00108.1, 2015b.

956   Knippertz, P., Fink, A. H., Deroubaix, A., Morris, E., Tocquer, F., Evans, M. J., Flamant, C.,

957   Gaetani, M., Lavaysse, C., Mari, C., Marsham, J. H., Meynadier, R., Affo-Dogo, A., Bahaga,

958   T., Brosse, F., Deetz, K., Guebsi, R., Latifou, I., Maranan, M., Rosenberg, 5 P. D., and

959   Schlueter, A.: A meteorological and chemical overview of the DACCIWA field campaign in

960   West Africa in June-July 2016, Atmospheric Chemistry and Physics, 17, 10 893–10 918,

961   https://www.atmos-chem-phys.net/17/10893/2017/, 2017.

962   Lack, D. A. and Cappa, C. D.: Impact of brown and clear carbon on light absorption enhancement,

963   single scatter albedo and absorption wavelength dependence of black carbon, Atmos. Chem.

964   Phys., 10, 4207–4220, doi:10.5194/acp-10-4207-2010, 2010.

965   Laing, J. R., Jaffe, D. A., and Hee, J. R.: Physical and optical properties of aged biomass burning
966   aerosol from wildfires in Siberia and the Western USA at the Mt. Bachelor Observatory, Atmos.
967   Chem. Phys., 16, 15185-15197, https://doi.org/10.5194/acp-16-15185-2016, 2016.

968   Lebel, T., Parker, D.J., Flamant, C., Bourles, B., Marticorena, M., Mougin, E., Peugeot, C.,
969   Diedhiou, A., Haywood, J.M., Ngamini, J.B., Polcher, J., Redelsperger, J.L., Thorncroft, C.D.:
970   The AMMA field campaigns: multiscale and multidisciplinary observations in the West African
971   region, Quarterly Journal of the Royal Meteorological Society, 136(S1), 8–33, 2010.

972   Lewis, K., Arnott, W. P., Moosmuller, H., and Wold, C. E.: Strong spectral variation of biomass
973   smoke light absorption and single scattering albedo observed with a novel dual-wavelength
974   photoacoustic instrument, J. Geophys. Res., 113, D16203, doi:10.1029/2007jd009699, 2008.

975   Lieke, K., Kandler, K., Scheuvens, D., Emmel, C., Von Glahn, C., Petzold, A., Weinzierl, B., Veira,
976   A., Ebert, M., Weinbruch, S., and SchÜTz, L.: Particle chemical properties in the vertical
977   column based on aircraft observations in the vicinity of Cape Verde Islands, Tellus B, 63, 497-
978   511, doi: 10.1111/j.1600-0889.2011.00553.x, 2011.

979   Liousse, C., Assamoi, E., Criqui, P., Granier, C., and Rosset, R.: Explosive growth in African
980   combustion emissions from 2005 to 2030, Environmental Research Letters, 9, 035003,
981   https://doi.org/10.1088/1748-9326/9/3/035003, 2014.

982   Liu, D., Taylor, J. W., Crosier, J., Marsden, N., Bower, K. N., Lloyd, G., Ryder, C. L., Brooke, J.
983   K., Cotton, R., Marenco, F., Blyth, A., Cui, Z., Estelles, V., Gallagher, M., Coe, H., and
984   Choularton, T. W.: Aircraft and ground measurements of dust aerosols over the west African
985   coast in summer 2015 during ICE-D and AER-D, Atmos. Chem. Phys., 18, 3817-3838,
986   https://doi.org/10.5194/acp-18-3817-2018, 2018.

987   Magi, B. I., Magi A., Hobbs P.V., Schmid B., and Redemann J., Vertical profiles of light scattering,
988   light absorption and single-scattering albedo during the dry, biomass burning season in
989   southern Africa and comparisons of in situ and remote sensing measurements of aerosol optical
990   depths, Journal of Geophysical Research, 108 (D13), doi:10.1029/2002JD002361, 2003.

991   Mallet, M., Nabat, P., Zuidema, P., Redemann, J., Sayer, A. M., Stengel, M., Schmidt, S.,
992   Cochrane, S., Burton, S., Ferrare, R., Meyer, K., Saide, P., Jethva, H., Torres, O., Wood, R.,
993   Saint Martin, D., Roehrig, R., Hsu, C., and Formenti, P.: Simulation of the transport, vertical
994   distribution, optical properties and radiative impact of smoke aerosols with the ALADIN
995   regional climate model during the ORACLES-2016 and LASIC experiments, Atmos. Chem.
996   Phys., 19, 4963-4990, https://doi.org/10.5194/acp-19-4963-2019, 2019.

997   Mann, G. W., Carslaw, K. S., Reddington, C. L., Pringle, K. J., Schulz, M., Asmi, A., Spracklen, D.
998   V., Ridley, D. A., Woodhouse, M. T., Lee, L. A., Zhang, K., Ghan, S. J., Easter, R. C., Liu, X.,

999 Stier, P., Lee, Y. H., Adams, P. J., Tost, H., Lelieveld, J., Bauer, S. E., Tsigaridis, K., van Noije,

1000 T. P. C., Strunk, A., Vignati, E., Bellouin, N., Dalvi, M., Johnson, C. E., Bergman, T., Kokkola,

1001 H., von Salzen, K., Yu, F., Luo, G., Petzold, A., Heintzenberg, J., Clarke, A., Ogren, J. A., Gras,

1002 J., Baltensperger, U., Kaminski, U., Jennings, S. G., O'Dowd, C. D., Harrison, R. M., Beddows,

1003 D. C. S., Kulmala, M., Viisanen, Y., Ulevicius, V., Mihalopoulos, N., Zdimal, V., Fiebig, M.,

1004 Hansson, H.-C., Swietlicki, E., and Henzing, J. S.: Intercomparison and evaluation of global

1005 aerosol microphysical properties among AeroCom models of a range of complexity, Atmos.

1006 Chem. Phys., 14, 4679-4713, https://doi.org/10.5194/acp-14-4679-2014, 2014.

1007 Mari, C. H., Cailley, G., Corre, L., Saunois, M., Attié, J. L., Thouret, V., and Stohl, A.: Tracing

1008 biomass burning plumes from the Southern Hemisphere during the AMMA 2006 wet season

1009 experiment, Atmos. Chem. Phys., 8, 3951-3961, https://doi.org/10.5194/acp-8-3951-2008,

1010 2008.

1011 Martinorena, B. and Bergametti, G.: Two-year simulations of seasonal and interannual changes of

1012 the Saharan dust emissions, Geophys. Res. Lett., 23, 1921-1924, 1996.

1013 Massoli, P., Kebabian, P. L., Onasch, T. B., Hills, F. B., and Freedman, A., Aerosol light extinction

1014 measurements by Cavity Attenuated Phase Shift (CAPS) Spectroscopy: Laboratory validation

1015 and field deployment of a compact aerosol particle extinction monitor, Aerosol Sci. Tech., 44,

1016 428–435, doi:10.1080/02786821003716599, 2010.

1017 McConnell, C. L., Highwood, E. J., Coe, H., Formenti, P., Anderson, B., Osborne, S., Nava, S.,

1018 Desboeufs, K., Chen, G., and Harrison, M. A. J.: Seasonal variations of the physical and optical

1019 characteristics of Saharan dust: Results from the Dust Outflowand Deposition to the Ocean

1020 (DODO) experiment, J. Geophys. Res., 113, D14S05, doi:10.1029/2007JD009606, 2008.

1021 McMeeking, G. R., Fortner, E., Onasch, T. B., Taylor, J. W. Flynn, M., Coe, H., and Kreidenweis,

1022 S. M.: Impacts of non-refractory material on light absorption by aerosols emitted frombiomass

1023 burning, J. Geophys. Res.-Atmos., 119, 2014JD021750,

1024 https://doi.org/10.1002/2014JD021750, 2014.

1025 Menut, L., Flamant, C., Turquety, S., Deroubaix, A., Chazette, P., and Meynadier, R.: Impact of

1026 biomass burning on pollutant surface concentrations in megacities of the Gulf of Guinea,

1027 Atmospheric Chemistry and Physics, 18, 2687–20 2707, https://doi.org/10.5194/acp-18-2687-

1028 2018, 2018.

1029 Mertes, S., Schröder, F., Wiedensohler, A.: The particle detection efficiency curve of the TSI 3010

1030 CPC as a function of the temperature difference between saturator and condenser, Aerosol

1031 Science and Technology, 23, pp. 257-261, 1995.

1032   Mita, A., Isono, K., Effective complex refractive index of atmospheric aerosols containing
1033   absorbing   substances,   J.   Meteorol.   Soc.   Jpn.,   58,   69-80,
1034   https://doi.org/10.2151/jmsj1965.58.1_69 1980.

1035   Myhre, G., Samset, B. H., Schulz, M., Balkanski, Y., Bauer, S., Berntsen, T. K., Bian, H., Bellouin,
1036   N., Chin, M., Diehl, T., Easter, R. C., Feichter, J., Ghan, S. J., Hauglustaine, D., Iversen, T.,
1037   Kinne, S., Kirkevåg, A., Lamarque, J.-F., Lin, G., Liu, X., Lund, M. T., Luo, G., Ma, X., van
1038   Noije, T., Penner, J. E., Rasch, P. J., Ruiz, A., Seland, Skeie, R. B., Stier, P., Takemura, T.,
1039   Tsigaridis, K., Wang, P., Wang, Z., Xu, L., Yu, H., Yu, F., Yoon, J.-H., Zhang, K., Zhang, H.,
1040   and Zhou, C.: Radiative forcing of the direct aerosol effect from AeroCom Phase II simulations,
1041   Atmos. Chem. Phys., 13, 1853-1877, https://doi.org/10.5194/acp-13-1853-2013, 2013.

1042   Petzold, A., Rasp, K., Weinzierl, B., Esselborn, M., Hamburger, T.,Dornbrack, A., Kandler, K.,
1043   Schutz, L., Knippertz, P., Fiebig, M.,and Virkkula, A.: Saharan dust refractive index and optical
1044   properties from aircract-based observations during SAMUM 2006,Tellus B, 61 118–130, 2009.

1045   Petzold, A., Veira, A., Mund, S., Esselborn, M., Kiemle, C., Weinzierl, B., Hamburger, T., Ehret,
1046   G., Lieke, K., and Kandler, K.: Mixing of mineral dust with urban pollution aerosol over Dakar
1047   (Senegal): impact on dust physico-chemical and radiative properties, Tellus B, 63, 619-634,
1048   doi: 10.1111/j.1600-0889.2011.00547.x, 2011.

1049   Petzold, A., Onasch, T., Kebabian, P., and Freedman, A.: Intercomparison of a Cavity Attenuated
1050   Phase Shift-based extinction monitor (CAPS PMex) with an integrating nephelometer and a
1051   filter-based   absorption   monitor,   Atmos.   Meas.   Tech.,   6,   1141–1151,
1052   https://doi.org/10.5194/amt-6-1141-2013, 2013.

1053   Pistone, K., Redemann, J., Doherty, S., Zuidema, P., Burton, S., Cairns, B., Cochrane, S., Ferrare,
1054   R., Flynn, C., Freitag, S., Howell, S., Kacenelenbogen, M., LeBlanc, S., Liu, X., Schmidt, K.
1055   S., Sedlacek III, A. J., Segal-Rosenhaimer, M., Shinozuka, Y., Stamnes, S., van Diedenhoven,
1056   B., Van Harten, G., and Xu, F.: Intercomparison of biomass burning aerosol optical properties
1057   from in-situ and remote-sensing instruments in ORACLES-2016, Atmos. Chem. Phys.
1058   Discuss., https://doi.org/10.5194/acp-2019-142, in review, 2019.

1059   Pokhrel, R. P., Wagner, N. L., Langridge, J. M., Lack, D. A., Jayarathne, T., Stone, E. A.,
1060   Stockwell, C. E., Yokelson, R. J., and Murphy, S. M.: Parameterization of single-scattering
1061   albedo (SSA) and absorption Ångström exponent (AAE) with EC / OC for aerosol emissions
1062   from biomass burning, Atmos. Chem. Phys., 16, 9549–9561, https://doi.org/10.5194/acp-16-
1063   9549-2016, 2016.

1064   Reid, J. S., Eck, T. F., Christopher, S. A., Koppmann, R., Dubovik,O., Eleuterio, D. P., Holben, B.
1065   N., Reid, E. A., and Zhang, J.: A review of biomass burning emissions part III: intensive optical

properties of biomass burning particles, Atmos. Chem. Phys., 5,827–849, doi:10.5194/acp-5-827-2005, 2005.

Roehrig, R., D. Bouniol, F. Guichard, F. D. Hourdin, and J. L. Redelsperger, The present and future of the west african monsoon: A process-oriented assessment of CMIP5 simulations along the AMMA transect, J. Clim., 26, 6471–6505, doi:10.1175/JCLI-D-12-00505.1, 2013.

Romonosky, D., S. Gomez, J. Lam, C. Carrico, A. Aiken, P. Chylek, and M. Dubey, Optical Properties of Laboratory & Ambient Biomass Burning Aerosols: Elucidating Black, Brown, & Organic Carbon Components & Mixing Regimes, J. Geophys. Res. Atmospheres, 124, doi:10.1029/2018JD029892, 2019.

Russell M., Zhang, S.-H., Flagan, R.C., Seinfeld, J.H., Stolzenburg, M.R., Caldow, R.: Radially classified aerosol detector for aircraft-based submicron aerosol measurements, Journal of Atmospheric and Oceanic Technology, 13, 598-609, 1996.

Ryder, C. L., Highwood, E. J., Rosenberg, P. D., Trembath, J., Brooke, J. K., Bart, M., Dean, A., Crosier, J., Dorsey, J., Brindley, H., Banks, J., Marsham, J. H., McQuaid, J. B., Sodemann, H., and Washington, R.: Optical properties of Saharan dust aerosol and contribution from the coarse mode as measured during the Fennec 2011 aircraft campaign, Atmos. Chem. Phys., 13, 303–325, https://doi.org/10.5194/acp-13-303-2013, 2013.

Ryder, C. L., Marenco, F., Brooke, J. K., Estelles, V., Cotton, R., Formenti, P., McQuaid, J. B., Price, H. C., Liu, D., Ausset, P., Rosenberg, P. D., Taylor, J. W., Choularton, T., Bower, K., Coe, H., Gallagher, M., Crosier, J., Lloyd, G., Highwood, E. J., and Murray, B. J.: Coarse-mode mineral dust size distributions, composition and optical properties from AER-D aircraft measurements over the tropical eastern Atlantic, Atmos. Chem. Phys., 18, 17225-17257, https://doi.org/10.5194/acp-18-17225-2018, 2018.

Sakamoto, K. M., Allan, J. D., Coe, H., Taylor, J. W., Duck, T. J., and Pierce, J. R.: Aged boreal biomass-burning aerosol size distributions from BORTAS 2011, Atmos. Chem. Phys., 15, 1633–1646, doi:10.5194/acp-15-1633-2015, 2015.

Sakamoto, K. M., Laing, J. R., Stevens, R. G., Jaffe, D. A., and Pierce, J. R.: The evolution of biomass-burning aerosol size distributions due to coagulation: dependence on fire and meteorological details and parameterization, Atmos. Chem. Phys., 16, 7709-7724, https://doi.org/10.5194/acp-16-7709-2016, 2016.

Sandradewi, J., Prevot, A. S. H., Weingartner, E., Schmidhauser, R., Gysel, M., and Baltensperger, U.: A study of wood burning and traffic aerosols in an Alpine valley using a multi-wavelength Aethalometer, Atmos. Environ., 42, 101-112, doi: 10.1016/j.atmosenv.2007.09.034, 2008.

Schladitz, A., Muller, T., Kaaden, N., Massling, A., Kandler, K.,Ebert, M., Weinbruch, S., Deutscher, C., and Wiedensohler, A.:In situ measurements of optical properties at Tinfou (Morocco) during the Saharan Mineral Dust Experiment SAMUM 2006,Tellus B, 61, 64–78, doi:10.1111/j.1600-0889.2008.00397.x, 2009.

Schuster, G. L., Dubovik, O., and Holben, B. N.:Angstrom exponent and bimodal aerosol size distributions, J. Geophys. Res., 111, D07207, doi:101029/2005JD006328, 2006.

Schwarz, J. P., et al., Coatings and their enhancement of black carbon light absorption in the tropical atmosphere, *J. Geophys. Res.*, 113, D03203, doi:10.1029/2007JD009042, 2008.

Seinfeld, J. H. and Pandis, S. N.: Properties of the Atmospheric Aerosol, in: Atmospheric Chemistry and Physics: From Air Pollution to Climate Change, 2nd ed., John Wiley & Sons, New Jersey, USA, 350–388, 2006.

Shin, S.-K., Tesche, M., Noh, Y., and Müller, D.: Aerosol-type classification based on AERONET version 3 inversion products, Atmos. Meas. Tech., 12, 3789–3803, https://doi.org/10.5194/amt-12-3789-2019, 2019.

Silva, S. and Arellano, A.: Characterizing regional-scale combustion using satellite retrievals of CO, NO2 and CO2, Remote Sensing, 9, 744, https://doi.org/10.3390/rs9070744, 2017.

Solmon, F., Mallet, M., Elguindi, N., Giorgi, F., Zakey, A., and Konare, A.: Dust aerosol impact on regional precipitation over western Africa, mechanisms and sensitivity to absorption properties, Geophys. Res. Lett., 35, L24705, doi:10.1029/2008GL035900, 2008

Stier, P., Schutgens, N. A. J., Bellouin, N., Bian, H., Boucher, O., Chin, M., Ghan, S., Huneeus, N., Kinne, S., Lin, G., Ma, X., Myhre, G., Penner, J. E., Randles, C. A., Samset, B., Schulz, M., Takemura, T., Yu, F., Yu, H., and Zhou, C.: Host model uncertainties in aerosol radiative forcing estimates: results from the AeroCom Prescribed intercomparison study, Atmos. Chem. Phys., 13, 3245-3270, https://doi.org/10.5194/acp-13-3245-2013, 2013.

Stohl, A., Eckhardt, S., Forster, C., James, P., Spichtinger, N., and Seibert, P.: A replacement for simple back trajectory calculations in the interpretation of atmospheric trace substance measurements, Atmos. Environ., 36, 4635–4648, 2002.

Vakkari, V., Kerminen, V. M., Beukes, J. P., Tiitta, P., van Zyl, P. G., Josipovic, M., Venter, A. D., Jaars, K.,Worsnop, D. R., Kulmala, M., and Laakso, L.: Rapid changes in biomass burning aerosols by atmospheric oxidation, Geophys. Res. Lett., 41, 2644–2651, doi:10.1002/2014gl059396, 2014.

Virkkula, A., Correction of the Calibration of the 3-wavelength Particle Soot Absorption Photometer (3λ PSAP), Aerosol Science and Technology, 44:8, 706-712, DOI: 10.1080/02786826.2010.482110, 2010.

1133 Wang, T., T. F. Cheung, Y. S. Li, X. M. Yu, and D. R. Blake, Emission characteristics of CO, NOx
1134 ,SO2 and indications of biomass burning observed at a rural site in eastern China, J. Geophys.
1135 Res., 107 (D12), 4157, doi:10.1029/2001JD000724, 2002.

1136 Weinzierl, B., Sauer, D., Esselborn, M., Petzold, A., Veira, A., Rose, M., Mund, S., Wirth, M.,
1137 Ansmann, A., Tesche, M., Gross, S., and Freudenthaler, V.: Microphysical and optical
1138 properties of dust and tropical biomass burning aerosol layers in the Cape Verde region—an
1139 overview of the airborne in situ and lidar measurements during SAMUM-2, Tellus B, 63, 589-
1140 618, doi: 10.1111/j.1600-0889.2011.00566.x, 2011.

1141 Wiedensohler, A., Orsini, D., Covert, D.S., Coffmann, D., Cantrell, W., Havlicek, M., Brechtel,
1142 F.J., Russell, L.M., Weber, R.J., Gras, J., Hudson, J.G., Litchy M.: Intercomparison study of
1143 size-dependent counting efficiency of 26 condensation particle counters, Aerosol Science and
1144 Technology, 27, 224-242, 1997.

1145 Yokelson, R. J., Crounse, J. D., DeCarlo, P. F., Karl, T., Urbanski, S., Atlas, E., Campos, T.,
1146 Shinozuka, Y., Kapustin, V., Clarke, A. D., Weinheimer, A., Knapp, D. J., Montzka, D. D.,
1147 Holloway, J., Weibring, P., Flocke, F., Zheng, W., Toohey, D., Wennberg, P. O., Wiedinmyer, C.,
1148 Mauldin, L., Fried, A., Richter, D., Walega, J., Jimenez, J. L., Adachi, K., Buseck, P. R., Hall,
1149 S. R., and Shetter, R.: Emissions from biomass burning in the Yucatan, Atmos. Chem. Phys., 9,
1150 5785-5812, https://doi.org/10.5194/acp-9-5785-2009, 2009.

1151 Zhong, M. and Jang, M.: Dynamic light absorption of biomass-burning organic carbon
1152 photochemically aged under natural sunlight, Atmos. Chem. Phys., 14, 1517-1525,
1153 https://doi.org/10.5194/acp-14-1517-2014, 2014.

1154 Zhai, J., Lu, X., Li, L., Zhang, Q., Zhang, C., Chen, H., Yang, X., and Chen, J.: Size-resolved
1155 chemical composition, effective density, and optical properties of biomass burning particles,
1156 Atmos. Chem. Phys., 17, 7481-7493, https://doi.org/10.5194/acp-17-7481-2017, 2017.

1157 Zuidema, P., Redeman, J., Haywood, J., Wood, R., Piketh, S., Hipondoka, M. and Formenti, P.:
1158 Smoke and clouds above the southeast Atlantic: upcoming field campaigns probe absorbing
1159 aerosols impact on climate, Bull. Am. Meteorol. Soc., doi: 10.1175/BAMS-D-15-00082.1,
1160 2016.

1161 Zuidema, P., Sedlacek III, A. J., Flynn, C., Springston, S., Delgadillo, R., Zhang, J., Aiken, A. C.,
1162 Koontz, A., Muradyan,P., and Zuidema, P.: The Ascension Island boundary layer in the remote
1163 southeast Atlantic is often smoky, Geophysical Research Letters, In Press, 4456–4465,
1164 https://doi.org/10.1002/2017GL076926, 2018.